

**BOW TIE SHAPED COPLANAR
WAVEGUIDE MICROWAVE RESONATORS
FOR SINGLE CELL DETECTION, FLOW
RATE MEASUREMENTS, AND NANOPORE
SENSING OF VIRUSES**

A THESIS SUBMITTED TO
THE GRADUATE SCHOOL OF ENGINEERING AND SCIENCE
OF BILKENT UNIVERSITY
IN PARTIAL FULFILLMENT OF THE REQUIREMENTS FOR
THE DEGREE OF
MASTER OF SCIENCE
IN
MECHANICAL ENGINEERING

By
Arda Seçme
September 2020

BOW TIE SHAPED COPLANAR WAVEGUIDE MICROWAVE
RESONATORS FOR SINGLE CELL DETECTION, FLOW RATE
MEASUREMENTS, AND NANOPORE SENSING OF VIRUSES

By Arda Seçme

September 2020

We certify that we have read this thesis and that in our opinion it is fully adequate,
in scope and in quality, as a thesis for the degree of Master of Science.

Mehmet Selim Hanay(Advisor)

Alper Demir

Barbaros Çetin

Approved for the Graduate School of Engineering and Science:

Ezhan Kardeşan
Director of the Graduate School

ABSTRACT

BOW TIE SHAPED COPLANAR WAVEGUIDE MICROWAVE RESONATORS FOR SINGLE CELL DETECTION, FLOW RATE MEASUREMENTS, AND NANOPORE SENSING OF VIRUSES

Arda Seçme

M.S. in Mechanical Engineering

Advisor: Mehmet Selim Hanay

September 2020

Measurement sensitivity of different biosensing applications can be enhanced by using the microwave resonators. In the first application, microwave sensors based on bow tie shaped coplanar waveguide (CPW) resonator was designed to detect single cells in real-time. While the resonator was kept at its resonance frequency, cells/particles were made a pass through the sensing electrodes and their frequency shift statistics were obtained. For each cell, the geometrical size that is obtained from the optical microscope was correlated to the electrical volume of the cell which was measured by the microwave signals. A linear relationship was observed between the electrical and geometrical volume of a cell. Dispersion caused by the device geometry was elucidated using the standard sized polystyrene microparticles. To observe the single-cell dynamic, a target cell was trapped around the sensing region, and its microwave response was continuously recorded. Then cells were treated with dimethyl sulfoxide (DMSO), a chemical accelerating dehydration, and a decline in the resonance shifts by time was observed as the cell lost total content.

Secondly, the same microwave design was patterned on a low-stress thin film membrane and used for flow rate measurements. When the flow is on, there were certain shapes continuously formed on the membrane and after a critical point pulsation of the membrane cause a shift in the resonance frequency. When the flow rate was increased, it was observed that these shapes formed faster so does frequency shifts in the resonance. Therefore, the effective flow rate could be correlated to the pulsation frequency of the membrane. Then, devices with different membrane size and different channel geometry were fabricated to span

different flow rate values. As a secondary sensing mechanism, the flow was given from the reset condition where there was no flow. In this case, the amount of frequency shift was related to the flow rate and a monotonically increasing relation was obtained. As a next step, instead of liquid, the air was pressurized to measure the flow rate. Airflow measurements have become important during the COVID-19 pandemic as the flow rate sensors are the most essential component of the ventilation machines. Using the secondary mechanism, frequency shifts induced by airflow were recorded and a linear relation was observed between the applied air pressure and frequency modulations.

In the last application, the sensing electrodes were patterned down to hundreds of nanometer apart to detect nanoparticles and biological samples such as polystyrene nanoparticles or viruses. A nanopore having a diameter around 400 nm was drilled on the membrane using focused ion beam (FIB) and analytes were translocated using electrokinetic motion. Since the events would be quick in electrokinetic motion, data were collected with CompactRIO (cRIO), however, when the PLL was running, there were spikes in cRIO for this reason after the resonator was locked to zero degrees, LabVIEW was stopped. Yet, since the resonator has low quality factor (≈ 100), the phase of the resonator dwells around zero degrees and still sensitive to translocations through the pore. In the control run, there were no precipitous jumps, however, when the particles were added sudden jumps induced by the particles were recorded. Therefore, can be optimized and proposed as a biophysical sensor to characterize single viruses.

Keywords: Microwave, Sensing, Single Cell, Flow Measurement, Single Virus Detection.

ÖZET

PAPYON ŞEKLİNDEKİ DÜZLEMDEŞ DALGA KILAVUZU MİKRODALGA REZONATÖRLERİ İLE TEK-HÜCRE TESPİTİ, AKIŞ HIZI ÖLÇÜMÜ, VE VİRÜSLERİN NANOGÖZENEKLE ALGILANMASI

Arda Seçme

Makine Mühendisliği, Yüksek Lisans

Tez Danışmanı: Mehmet Selim Hanay

Eylül 2020

Biyoalgılama uygulamalarının ölçüm hassasiyeti mikrodalga rezonatörleri ile arttırılabilir. İlk uygulamada papyon şeklindeki düzlemdeş dalga kılavuzu tabanlı rezonatörler tasarlanarak gerçek zamanlı tek-hücre tespiti yapılmıştır. Tımlatıcı, rezonans frekansında salınım yaparken, hücreler/parçacıklar algılayıcı elektrotlardan geçirilerek, hücrelerin/parçacıkların frekans kaymasındaki oluşturduğu değişimler kaydedilmiştir. Her bir hücre için, optik mikroskoptan elde edilen geometrik boyut, mikrodalga ölçümlerinden elde edilen elektriksel boyut ile ilişkilendirilmiştir ve geometrik boyut ile elektriksel boyut arasında çizgisel bir ilişki gözlenmiştir. Üretilen cihazın yapısından kaynaklanan dağılımlar, standart boyutlu polistren parçacıklar kullanılarak ortaya çıkarılmıştır. Tek hücre dinamiğini gözlemlemek için algılayıcı elektrotlar etrafında hedef bir hücre kapanlamış ve hücrenin mikrodalga tepkisi devamlı şekilde kaydedilmiştir. Daha sonra hücreler, su kaybını hızlandıracak Dimetil sülfoksit (DMSO) ile işleme tabii tutulmuş ve zamanla, hücrenin içerisindeki malzemenin azalması nedeniyle, rezonanstaki kayma miktarlarının azaldığı gözlemlenmiştir.

İkinci uygulamada, aynı mikrodalga tasarımı, düşük gerilimli ince film membran üzerine desenlenmiş ve akış hızı ölçümlerinde kullanılmıştır. Akış, aktif hale geldiğinde membran üzerinde tekrarlı şekillerin oluştuğu ve kritik bir noktadan sonra membranın nabız atma şeklindeki hareketinin frekans kaymasında değişime neden olduğu kaydedilmiştir. Akış hızı arttırıldığında ise membran üzerindeki şekillerin daha hızlı oluştuğu, dolayısıyla frekanstaki kaymaların da daha hızlı olduğu gözlemlenmiştir. Bu nedenle efektif akış hızı, membranın nabız atma frekansına ilişkilendirilebilir. Daha sonra, farklı membran ve kanal ölçülerinde

aygıtlar üretilerek farklı akış hızı değerleri taranmıştır. İkincil bir ölçüm tekniği olarak, akış sıfırdan verilmiştir. Bu kez, akış hızı ile frekans kayması arasında tekdüze bir artış elde edilmiştir. Bir sonraki aşamada, mikrokanala sıvı yerine hava basınçlanarak akış hızı ölçülmüştür. Hava akış hızı ölçüm sensörleri, havalandırma makineleri için büyük önem arz etmektedir, nitekim havalandırma cihazları da COVID-19 pandemisi süresinde önemli hale gelmiştir. İkincil ölçüm tekniğini kullanarak frekans kaymaları kaydedilmiş ve uygulanan basınçla frekans kiplemeleri arasında çizgisel bir ilişki gözlemlenmiştir.

Son uygulamada, algılayıcı elektrotlar yüzlerce nanometre aralıklı üretilerek nanoparçacıklar ve biyolojik numuneler, örneğin polistren nanoparçacık ve virüsler, tespit edilmiştir. Odaklanmış iyon ışını yöntemiyle membran üzerinde 400 nm çapında bir nano gözenek açılarak elektro kinetik yöntemle analitlerin bu gözenekten geçmeleri sağlanmıştır. Elektro kinetik yöntemle geçirilen analitlerin oluşturacağı kaymalar çok hızlı olacağından ötürü CompactRIO (cRIO) cihazı kullanılarak data toplanmıştır. Fakat LabVIEW üzerinden kontrol edilen faz kenetleme döngüsü çalışırken, cRIO bilgisinde sıçramalar görüldüğünden ötürü rezonatorün fazı sıfır derece kitlendikten sonra LabVIEW durdurulmuştur. Üretilen cihazın kalite faktörü düşük olduğundan ötürü (≈ 100) faz değeri sıfır etrafında salınım yapmaya devam ederken analitlerin nanogözenekten geçişlerinden doğacak değişimlere de tepki verebilecek kadar duyarlıdır. Kontrol turunda, fazda herhangi bir ani değişim gözükmezken parçacıklar eklendikten sonra rezonatorün fazında ani sıçramalar kaydedilmiştir. İyileştirme sürecinden sonra mikrodalga rezonatörlerinin tek-virüs karakterizasyonu amacıyla biyofiziksel sensör olarak kullanılması önerilebilir.

Anahtar sözcükler: Mikrodalga, Algılama, Tek-Hücre, Akış Hızı Ölçümü, Tek-Virüs Tespiti.

Acknowledgement

First of all, I would like to thank my family who has always supported, believed, and did the best for me.

I am thankful & grateful to my supervisor, Dr. Selim Hanay, for his continuous guidance on me. He has given me several great research opportunities during my undergrad and master studies, but more importantly, he has envisioned me to always make myself better. He has been more than a supervisor and inspiration for my future career. I would like to also thank Prof. Alper Demir and Assoc. Prof. Barbaros Çetin for their contribution to my thesis committee.

I am also thankful to our postdoc, Dr. Hadi Pisheh, who has ceaselessly helped me in all the projects described in the thesis. I would like to thank for his guidance and help in the cleanroom fabrication, but more importantly, I am grateful for the talks he gave to motivate me. I would like to thank all other Hanay group members: Hande Aydoğmuş, Mehmet Kelleci for their guidance; Dilara Uslu, Berk Küçüköğlü, Tufan Erdoğan, and Berke Demiralp for their help in the projects. Special thanks to Özge Akbulut for her perfect guidance in cell culture.

My most special thanks to my groupmates from undergrad years: Erkan Aksoylu, Emre Aydemir, and Berkay Alp Çakal. As Atletiko Makine, we have ranked first or the best in all the projects in undergrad courses. Vamos Atletiko! I am grateful to my officemates: Tamer Taşkıran, Alper Topuz and Redion Xhepa for their great friendship over 2 years. I am also thankful to my friends in Ankara: Can Tüysüz, Semra Ay.

I would like to also thank European Research Council (ERC) for their generous financial support to make all these projects possible.

”Our true mentor in life is science”

Contents

- 1 Introduction** **1**
 - 1.1 Single Cell Detection 1
 - 1.2 Nanomechanical Flow Rate Sensor 3
 - 1.3 Nanopore Sensing of Viruses 5
 - 1.4 Thesis Outline 7

- 2 Single Cell Detection** **9**
 - 2.1 Resonant Microwave Sensor Design 10
 - 2.2 Fabrication Steps 11
 - 2.3 Experimental Procedure 13
 - 2.3.1 Electronic Measurement 14
 - 2.3.2 Cell Culturing 17
 - 2.4 Experimental Results 20
 - 2.4.1 Size Correlation Experiments 20

2.4.2	Calibration Experiments with Microparticles	23
2.4.3	Single Cell Trapping	25
2.4.4	DMSO Experiments	27
2.5	Analytical Calculations for Frequency Shifts	28
3	Nanomechanical Flow Rate Sensor	32
3.1	Device Fabrication	33
3.2	Experimental Setup	35
3.3	Experimental Results	36
3.3.1	First Sensing Mechanism: Pulsation Frequency	39
3.3.2	Secondary Sensing Mechanism: Reset Condition	42
3.3.3	Air Flow Experiments with Secondary Mechanism	45
4	Nanopore Sensing of Viruses	48
4.1	Device Fabrication	49
4.2	Experimental Setup	51
4.3	Nanopore and I-V Curve Measurements	52
4.4	Experimental Results	54
4.4.1	Gold Nanoparticle Experiments	54
4.4.2	Design Optimization & Faster Data Recording	56

<i>CONTENTS</i>	x
4.4.3 Polystyrene Particle Experiments	58
4.4.4 Felocell Vaccine Experiments	61
5 Conclusion & Future Perspective	64
5.1 Single Cell Detection	64
5.2 Nanomechanical Flow Rate Sensor	66
5.3 Nanopore Sensing of Viruses	67
A Supplementary Materials for Cell Detection Part	81
B Supplementary Materials for Flow Sensor Part	85

List of Figures

2.1	Dimensions of the designed resonator	10
2.2	Electric field distribution	11
2.3	Fabrication steps	12
2.4	Experimental setup	14
2.5	S21 VNA response	15
2.6	Measurement circuitry	16
2.7	Plate sizes & buffer amounts	18
2.8	Size correlation	20
2.9	Size correlation experiments	22
2.10	Positional dependence	24
2.11	Image processing algorithm	25
2.12	Single cell trapping	26
2.13	DMSO experiments	28

2.14	Shift estimation on experimental data	31
3.1	Fabrication steps of the flow rate sensor	33
3.2	Layers of flow rate sensor	35
3.3	Experimental setup	36
3.4	State transitions	37
3.5	Microwave response of the flow rate sensor	38
3.6	Full spectrum of the microwave response	39
3.7	Pulsation frequency with 3 different devices	41
3.8	Frequency shifts during pulsations	42
3.9	Reset condition	43
3.10	Minimum sensitivity level for the secondary mechanism	44
3.11	Repeatability of the secondary sensing mechanism	45
3.12	Membrane fabricated for air flow experiments	46
3.13	Frequency response vs Applied air pressure	47
4.1	Flow schematics for fabrication	49
4.2	Electrodes after EBL process	50
4.3	Fabricated electrodes	51
4.4	Experimental configuration	52

4.5	I-V curve measurement	53
4.6	Gold nanoparticle experiment	55
4.7	Histogram of gold nanoparticles	55
4.8	Design improvement	56
4.9	S21 VNA response after optimizations	57
4.10	100 nm polystyrene particle	58
4.11	Control over electrokinetic motion	59
4.12	Histogram for 100 nm polystyrene particle	59
4.13	50 nm polystyrene particle	60
4.14	Histogram for 50 nm polystyrene particle	61
4.15	Felocell CVR experiment	62
4.16	Histogram of the phase shifts in Felocell CVR experiment	62
A.1	Photolithography mask used for cell detection & flow rate sensor	81
A.2	An example of device after cleanroom fabrication	82
A.3	Working steps of the custom-built image processing algorithm	83
A.4	Boxplots for the Histogram in Figure 2.12	83
A.5	Frequency shift trend obtained with different cells and devices	84
B.1	An example of block diagram used for automatically adjusting flow rate using Fluent software	85

List of Tables

2.1	Content of the DMEM solution	17
2.2	Buffer amounts according to the plate size	18

Chapter 1

Introduction

This thesis introduces microwave resonators for 3 different applications: first, a microwave sensor to detect single cells will be introduced, followed by a flow rate sensor based on nanomechanical membranes and lastly, virus detection with microwave signals integrated with solid-state nanopore will be explained.

1.1 Single Cell Detection

In the first application, a platform based on microwave sensing is proposed to detect single cells and observe their morphology in real-time. The main motivation is to develop a platform that can enhance the effectiveness of the cancer treatment. In chemotherapy, for instance, different drugs are simultaneously inserted into the patient's body, however, the question of which drug is the most effective is still vague and may change over the different phase of the disease. At this point, using the proposed platform, each drug could be tested solely on a single cell at different phases and the most efficient drug treatment can be determined.

Personalized medicine and early diagnosis of the diseases [1, 2] can be examined by high speed measurement of the size of a cell . Quantitative phase microscopy [1, 3, 4] can be used to target a cell and observe its dynamics continuously.

However, a platform having a smaller form factor, lower cost, and ease of use is integral for a point-of-care applications. For these reasons, there are several sensor technologies being developed to detect and measure the size of a single cell [5, 6, 7, 8, 9, 10]. In fact, some technologies also observe fast mass accumulations at a single-cell level [11] and drug response of the cancer cells derived from different patients [12].

As the mass indicates the metric of the total material inside a cell, the aforementioned sensor technology focuses on the mass measurement at the single-cell level [13]. Micromechanical structures, which are highly sensitive to effective mass changes induced by external effects, are being used to detect to observe changes in the mass of a cell [14, 15, 16]. Yet, the fluidic media impairs the performance of the sensor due to viscous dissipation and low diffusion rates. To forestall these problems, resonators based on suspended microchannels have been developed and operate under vacuum conditions while the fluid was encapsulated. This technology was first developed [5, 17, 18] and optimized [6, 7, 19, 20, 21] by Manalis group, however, several other research groups are also developing a similar technology [22, 23, 24, 25, 26, 27]. The major challenge in this technology is the fabrication of a hollow, small-sized channel on the cantilever which is coercive and increases the cost of each sensor.

The total content inside a cell can be determined by other parameters as well, for instance, the polarization density of a cell differs from the external medium thanks to the fact that the cell produces biochemical components, e.g. cytoskeletal proteins and phospholipids, and maintains the unbalanced & electrolytes in its cytosol compared to the external environment. The difference in the polarization stems from the total content inside the cell and this difference affects the dielectric constant & capacitance of the cell when it is superseded with the fluid. Therefore, capacitance changes induced by a single cell can be detected by a resonant electrical sensor that can resolve size changes in single cells. However, the effect of Debye screening and polarization on the membrane becomes dominant at low frequency, i.e. < 1 GHz; above 1 GHz electrolyte ions cannot move and hydrogen bonds can be polarized up to 20 GHz. Utilizing this fact, a large contrast difference was obtained between the medium, where the cell

flows, and polymers inside the cell (e.g. cytoskeleton and organelles). Thanks to this contrast, microwave-based resonators can be also used to measure cells [28, 29, 30, 31, 32, 33].

In this thesis, a microwave resonator is proposed to detect cells and answer to the question of whether the electrical volume of a cell (microwave response), correlates to the geometrical size of a cell (optical microscope images) was investigated. By synchronizing the optical imaging with microwave sensing, it was verified that the electrical and geometrical volume of a cell is correlated. With results obtained, Microfluidics-Integrated Microwave Sensors (MIMS) can be proposed as a new sensor technology for single-cell biophysics with a lower cost and easier fabrication steps.

1.2 Nanomechanical Flow Rate Sensor

In the second application, microwave sensing is integrated on a nanomembrane to determine the effective flow rate inside a microchannel. In this way, more sensitive flow rate measurement was aimed at.

Mechanisms of nanomechanical resonators working in a fluid [34, 35, 36] and suspended microchannel resonators filled with fluid [37, 38, 39] have been highlighted to understand the interaction between fluid flow and mechanical structures. In these studies, the mechanical bridge was driven externally and the fluid was the source of dissipation and changed the effective mass of the element. However, as in the case of fluttering of a flag or paper, simple fluid flow can also induce an instability [40, 41, 42], and excite the motion instead of damping. To observe flow-induced instability, a low-stress silicon nitride (Si_3N_4) membrane having 220 nm thickness was elaborated under the fluid flow. While one side of the membrane was in the interaction with the fluid within a microfluidic channel, the other side was in touch with the room conditions. When the flow was on, cyclic patterns were observed on the membrane and the cycling rate was proportional to the effective flow rate which can be proposed as an on-chip flow rate

measurement sensor.

Flow rate measurement is crucial for several biomedical applications of microfluidics such as the adhesion rate of the cells on a substrate, concentration of a cell inside a test volume, and sorting the cells according to their size. For organ-on-chip and tumor on-chip applications, cells should be supplied with the optimized amount of nutrition to maintain their viability. Doses of the tested drug should be inserted to the cell in a controlled fashion to obtain the most accurate cellular response [12, 43]. In discrete microfluidics area, with a finely controlled flow rate, droplets having similar composition can be generated at different flow rate value [44, 45, 46]. In most of these studies, syringe pumps or peristaltic pumps are being used, yet, fluctuations and low response time in those devices decrease the productivity of the target application. Commercial flow rate sensors are placed outside of the target channel, generally in between the flow source and the chip. The robust on-chip flow rate sensor should be within the microchannel to determine the effective flow rate accurately.

Commercial flow rate sensors work based on different mechanisms: thermal, capacitive, and optical sensing. Thermal sensors work based on hot wire anemometer where there is a heat source in the middle, two temperature sensors are placed at two different locations, and based on the speed of the heat convection profile, the flow rate is determined [47, 48, 49, 50]. Capacitive based flow sensors work by shifting the thickness of the dielectric material or the surface of the electrode [51]. Different techniques are used in optical flow sensors to measure the flow rate. Some examples are microbubble image velocimetry [52, 53], microparticle velocimetry [54, 55] and Doppler Velocimetry [56, 57]. Optofluidic sensors are also used for flow rate measurement and the working mechanism is based on the deflection of the cantilever induced by drag force. Minimum detectable flow rate was $1.3 \mu\text{L}/\text{min}$ [58] with an incremental change of $4 \mu\text{L}/\text{min}$.

Mechanical flow rate sensors are based on the perforated cantilever with variable sized holes and changes in the flow rate are quantified by correlating the deflection of the cantilever to the flow [59]. With those structures, an astonishing flow rate in the order of nL/min was achieved, however, the fabrication

and operation of such perforated cantilever are stringent as there is a need for directing the flow through a nanostructure. Also, to readout the deflection of the cantilever, a microscope is needed. There are several other flow sensors integrated with electronics operating in the radio frequency reported [60, 61]. In a recent work Zarifi et. al.[61] utilized the deflection of a PDMS layer and coupled it to a microwave circuitry. The sensitivity of this method is $0.5 \mu\text{L}/\text{min}$.

In this thesis, observation of the flow-induced states led to converting it into a flow sensing mechanism by patterning a CPW microwave sensing electrodes on top of the membrane. Changes in the resonance frequency induced by the membrane pulsations were recorded at different flow rate values. Different sized membranes were employed to span fine and coarse flow profile. At the end of the experiments, the microwave integrated sensor could detect a minimum flow rate of $0.4 \mu\text{L}/\text{min}$ with an incremental change of $0.1 \mu\text{L}/\text{min}$.

1.3 Nanopore Sensing of Viruses

In the third application, nanopore sensing is utilized to detect and characterize single molecules using microwave signals. Nanopores are used for Single-Molecule/DNA sequencing, detection of biological analytes [63]. Recently, the field of nanopore sensing has attracted wide attention thanks to high sensitivity and high throughput at low cost offered by the sensing modality [62]. Furthermore, the ongoing COVID-19 pandemic has shown a need for low cost and point-of-care biosensors. With the proposed technique, testing capacity could have been increased by using such a physical sensor.

Nanopore DNA sequencing works as follows: each nucleotide passing through the pore has a different amplitude and duration observed through the current which can be then converted into DNA sequencing information [64, 65, 66, 67]. Recently, nanopore sequencing is highlighted as it is PCR & label-free, can read long chains, and gives high throughput. These features facilitate the genome reading procedure and nominate the nanopore technique for personal genome uses

[68, 69, 70]. More importantly, as nanopore sequencing engenders fast results at low costs, it is also useful for on-site diagnosis of infection such as COVID-19. In fact, Ebola samples that were collected on-site in Africa were detected by a nanopore sequencer [71].

Biological modifications caused by a disease or a drug delivery modulates the concentration of a protein and also its expression. Using nanopore sensing, these modifications can be quantified [72, 73]. While a protein passes through a nanopore, constrictions inside the pore can excite protein unfolding, denaturing, and translocation [74]. With this, the detection of the thermal unfolding of a protein can be examined. In addition to sensing, nanopores can be used for protein sequencing as well [75, 76].

Nanopore applications mentioned so far were performed by bio-nanopores. Sensing modality can be enhanced by the integration of a functional structure or a detection method using solid-state nanopores. In a recent work [77], the solid-state nanopores integrated with macromolecular crowding technique were used to detect proteins and DNA plasmids. Optical detection circuitry can also be built around the nanopore, and when a target molecule flow through the pore, optical signals were recorded using optical detectors [78, 79]. Optical nanopore sensing enhanced with plasmonic nanopore can identify DNA sequencing as well [80, 81, 82]. Nanopores can be also co-integrated with force measurement techniques such as atomic force microscopy, magnetic tweezers, and optical trapping by controlling the applied electrophoretic force on a charged analyte by the electric field generated. The detected signals are force signals which are correlated to molecular interaction between the pore and analytes during the passage [83].

As the key components of any nanopore/channel-based application, solid-state type membrane can be used thanks to its advantages of excellent durability, robustness, as well as seamless integration with existing semiconductor and microfluidics systems. For a sensitive measurement with nanopores, it is crucial to match the size of the pore to the size of the analyte, so that the analyte blocks almost the entire nanopore and induces higher conductivity change across the nanopore. To avoid this stringent condition between the size of the nanopore

and the analyte, resonant microwave circuitry was built around the solid-state nanopore. The fabrication of the sensor is also simple compared to suspended graphite [84] and nanoribbon [85] sheets, as well as, mechanically controlled break junctions (MCBJ) [86, 87, 88].

Similar microwave circuitry has been built by Bhat et. al. [89] using a vector network analyzer as a measurement tool and the nanopore was drilled by laser ablation. The pore size reported was $2\ \mu\text{m}$ and polystyrene particles having a size of $500\ \text{nm}$ and $1\ \mu\text{m}$ were detected. In another study [90], viruses were detected solid-state nanopores yet the sensing modality was resistive pulse sensing. In this thesis, a PLL circuitry was integrated around the nanopore so that continuous microwave measurement was enabled. In the experiments, nanoparticles and viruses were translocated using electrokinetic motion, and each particle/virus induced a shift in the resonance.

1.4 Thesis Outline

This thesis explains three different applications of the microwave resonator therefore it has 3 different chapters: Single Cell Detection, Nanomechanical Flow Rate Sensor, Nanopore Sensing of Viruses. In the first chapter for each application: motivation, detailed literature review, and novelty is explained.

In Chapter 2, details of the single-cell detection is explained starting with the device design and its fabrication. Then, the experimental setup and procedure are explained. Experimental results with size correlation, particle experiments, single-cell trapping, and DMSO experiments are illustrated.

In Chapter 3, the same microwave design in Chapter 2 was patterned on a nanomechanical membrane to convert membrane topology to determine the effective flow rate. First, the detailed fabrication procedure of the sensor was explained then the experimental setup was illustrated. In the experiments, two

different sensing mechanisms were used: Pulsation Frequency and Reset Condition. Initial experiments were tested by pressurizing DI water using both mechanisms, then the air was blown through the channel, and using the secondary mechanism frequency shifts were recorded.

In Chapter 4, a similar microwave design was used, however, this time electrodes were only hundreds of nanometer apart. A nanopore was drilled on the membrane and by using electrokinetic motion analytes were driven through the pore. For the experiments, gold nanoparticles, polystyrene particles, vaccine viruses were employed.

In Chapter 5, for all chapters summary of the work was given and some potential improvements and future applications were proposed.

Chapter 2

Single Cell Detection

The first application of bow tie coplanar waveguide (CPW) resonator is to detect individual cells without any labeling process in real-time. The proposed platform can observe the morphology of a single cell over time. In fact, the current COVID-19 pandemic has shown that low cost and point-of-care biosensors are essential. Testing capacity could have been increased by using physical sensors.

In the literature survey part, efforts to detect individual cells using microwave signals were reported [28, 29, 30, 31, 32, 33]. However, there were not many studies that relate microwave signals to the optical image. This study integrates microwave detection & optical imaging and differs from two commonly used techniques: coulter counters and suspended microchannel resonator. First, coulter counters measure the conductance change induced by a cell through a constriction, however, this constriction should closely match to cell size [91] and what is measured is the cross-section of the sample rather than its actual size. Since it only considers the conductance change, other particles such as dust and bacteria inside the electrolyte cannot be distinguished. Secondly, suspended microchannel resonators require complex fabrication steps, and a vacuum system required for sensitive measurement limits the widespread usage. Typically, optical readout techniques are employed in the measurement which increases the form factor of the technology.

2.1 Resonant Microwave Sensor Design

The designed sensor is based on bow tie CPW where the electric field is generated planar rather than out of the plane as in the case with microstrip line based resonators. To enhance the sensitivity of the measurement, signal and ground electrodes were separated by a distance down to cellular size scale ($\approx 50 \mu\text{m}$).

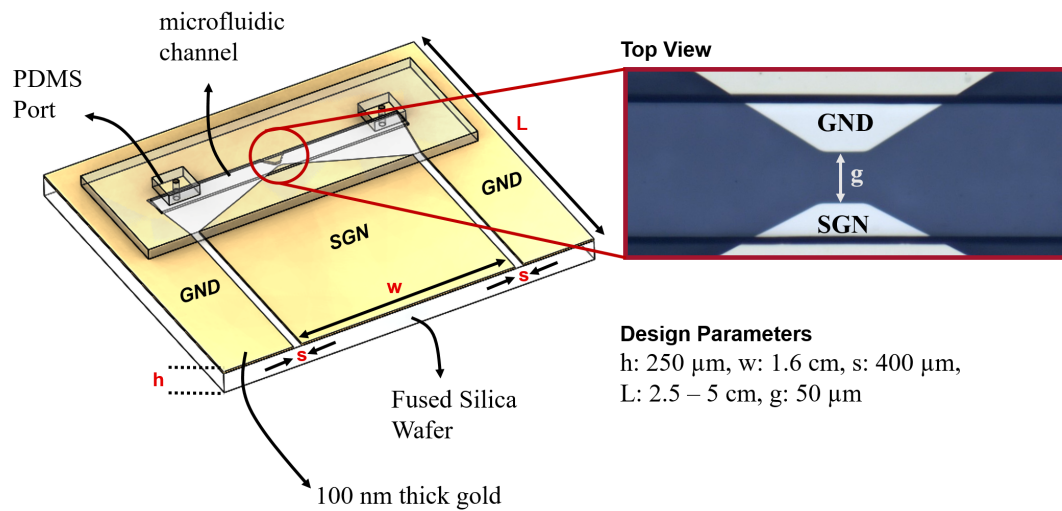


Figure 2.1: Dimensions of the designed resonator

For reducing the losses and noise level due to impedance mismatch with the measurement circuitry, design parameters were calculated such that the overall impedance matched to 50Ω . Figure 2.1 shows the details of the device dimensions.

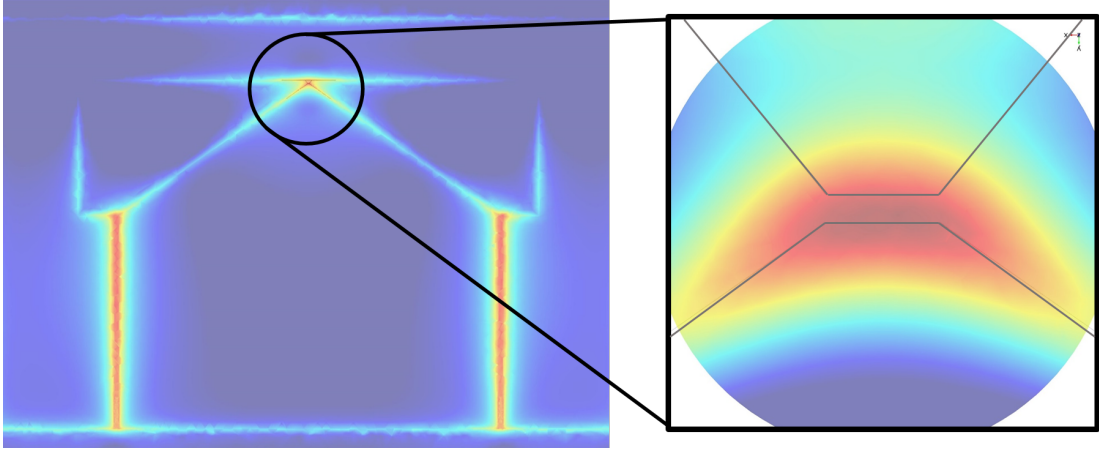


Figure 2.2: Electric field distribution

Same dimensions were exported to COMSOL to illustrate the electric field distribution. Figure 2.2 illustrates an example of normalized electric field distribution at 2.1 GHz resonance. As the signal and ground lines converge, electric field is intensified.

2.2 Fabrication Steps

Fabrication of the sensor consists of two sub-fabrication steps: chip fabrication & soft lithography. For the chip fabrication, 250 μm thick 4 inch fused silica wafer was diced into half and coated with the photoresist (AZ-5214) spin speed of 1000 rpm for 20 seconds. Then, the designed mask (Figure A.1) was used and aligned on the photoresist coated wafer and upon UV exposure polymer chains were weakened. Exposure parameters were as follows: Proximity & Separation: 200 μm , Thickness of the Resist: 1.3 μm , Dose: 150 mJ/cm^2 . In Appendix A, Figure A.1, the mask used in photolithography is illustrated with 4 different sensing gaps: 10, 20, 30, 50 μm for the same bow tie CPW design having 50 Ω impedance.

To fully obtain the desired pattern, the developer (AZ 400K, ratio 4:1) was

prepared and about 40 seconds, the chip was dipped into the developer solution. Then the sensing region was checked under the optical microscope unless the gap was obtained the chip was dipped into the developer solution for additional 10-20 seconds Figure 2.3a illustrates the schematic representation of the chip after the photolithography step. Once the bow tie pattern was obtained, the chip was placed inside the thermal evaporator. First, it was coated 10 nm Chromium for better sticking of Gold, then 100 nm Gold was coated. Afterwards, the chip was immersed into the acetone bath and left for liftoff for about 1-2 hours. Signal and ground paths were obtained on the chip as in Figure 2.3b.

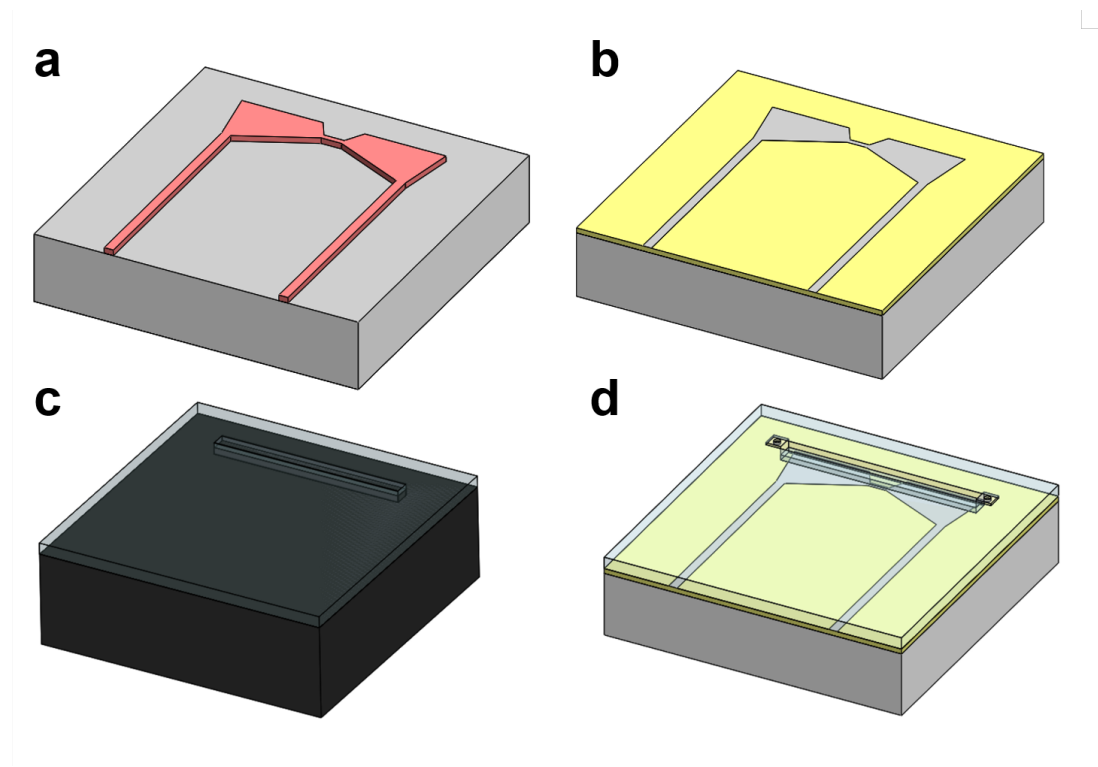


Figure 2.3: Fabrication steps

In the second part of the fabrication, a full Si wafer was used to prepare a mold for Polydimethylsiloxane(PDMS) microchannel fabrication. SU-8 (MicroChem 2050) was poured on to wafer and two steps of the spin coating were operated. In the first spin 500 rpm & 10 seconds, then 2000 rpm & 30 seconds was used. The wafer was left for soft baking for about 20 minutes at 95°C. After soft bake, the

wafer was UV exposed with the desired microchannel mask with the following exposure parameters: Proximity & Separation: 999 μm , Thickness of the Resist: 200 μm , Dose: 250 mJ/cm^2 . Next, the wafer was left for post-exposure bake for 10 minutes at 95°C and if the exposure was successful, patterns become visible within a minute during post-baking. Once the post-baking was performed, the wafer was developed using SU8 developer for 15 minutes. To check the development, isopropyl alcohol can be sprayed, if the color of the wafer changes to white, continue rinsing into the developer solution. Once the SU8 mold was ready, PDMS (Sylgard 184, 10:1) was prepared to pour into the mold and baked for half an hour (Figure 2.3c). By following the aforementioned fabrication parameters, at the end, the height of the channel will be around 100 - 120 μm .

When PDMS was cured, it was peeled from the mold, and using oxygen plasma, fabricated chip and PDMS channel was bonded. Plasma bonding parameters are as follows: RF Power: 83 Watt, O_2 : 25 sccm, N_2 : 5 sccm, Chamber & Substrate Temperature: 30°C. PDMS with microchannel was aligned to the electrodes under a microscope. The channel was juxtaposed to the sensing region manually and two PDMS ports were also bonded to the inlet and outlet ports for rigid tubing connection (Figure 2.3d). There can be some air stuck between the chip and PDMS, to get rid of those, the fabricated chip was placed on a hot plate overnight at 80°C to achieve a better bonding at the interface of PDMS & fused silica chip with gold patterns. Sides of the PDMS ports were sealed with a secondary PDMS, the aim of this is to maintain the connection of PDMS ports on PDMS. As the tubing is inserted/extracted this bonding degrades over time, however, this secondary sealing enables flexibility for repetitive tubing connections. In Appendix A, Figure A.2, shows an example of the fabricated chip after the cleanroom process.

2.3 Experimental Procedure

The experimental setup consists of 3 main subsystems: electronic measurement, microfluidics, and optical imaging (Figure 2.4). The fabricated chip was placed

on the microscope stage with all necessary electronic and microfluidic connections and it was encapsulated inside a Faraday cage to forestall microwave interference from external sources. A pressure controller (Fluigent; MFCS) was used to pressurize air to the reservoir to transfer cells to the sensing region. Here, the syringe pump was not used so the frequency shifts do not stem from the pulsations occurring in the syringe pump mechanism. In the meantime, incubated cell lines were passaged and added to the reservoir just before the experiment starts.

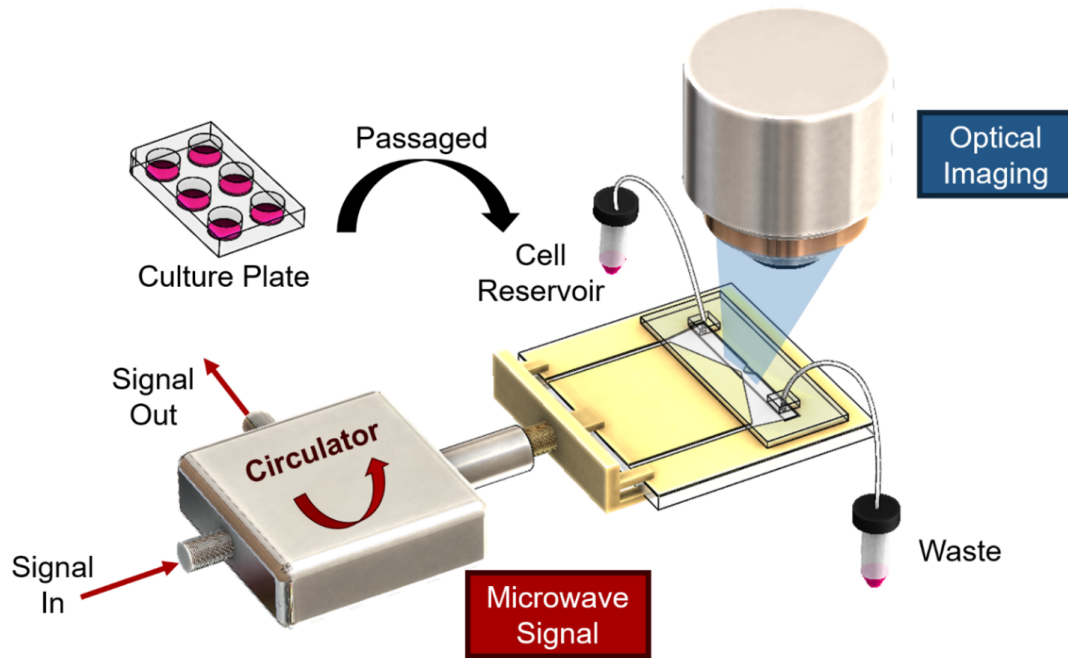


Figure 2.4: Experimental setup

2.3.1 Electronic Measurement

Initially, the resonance frequency of the microwave sensor was determined on the Vector Network Analyzer (VNA) by considering the single port measurement with S11 (or S22) parameter. S11 resonance of the designed resonator turned out to be between 2-3 GHz, so a circulator that operates in the interval of 2-4 GHz was employed to read S11 response of the sensor. An example of S21 response of the sensor when the circulator was inserted, is illustrated in Figure 2.5 having

resonance at 2.12 GHz. The quality factor of the resonator in Figure 2.5 is around 75.

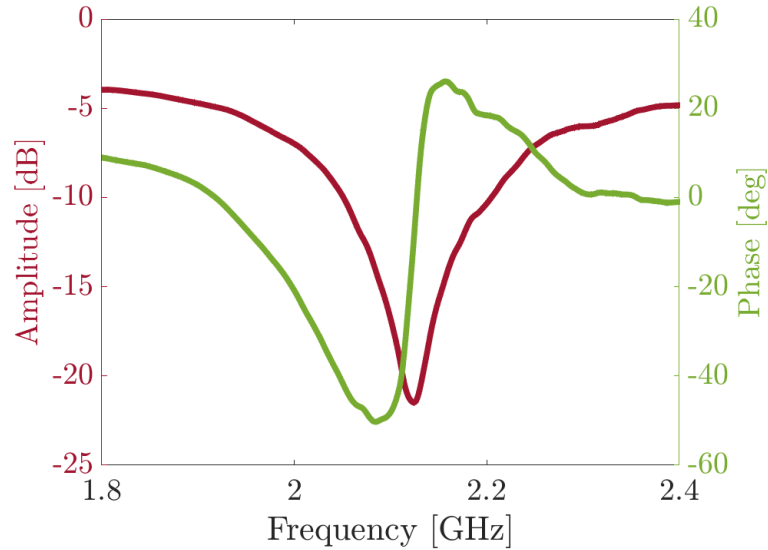


Figure 2.5: S21 VNA response

For the electronic measurement, narrow-band phase-sensitive detection circuitry was employed. Phase-sensitive detection was performed using lock-in amplifier, however, the upper-frequency limitation of the lock-in amplifier (5 MHz) requires an external heterodyne RF circuitry operating around the resonance frequency of the microwave resonator i.e. 2 - 4 GHz. For this reason, the driving signal from the signal generator, which is in the GHz range, was first upconverted with the constant frequency signal output from the lock-in amplifier (e.g. 2.5 MHz), then similarly downconverted.

Using Phase Locked Loop (PLL), the resonator has been continuously kept at its first resonance mode. PLL has been controlled through LabVIEW with a custom-built code that can read the demodulated signal from the lock-in amplifier, any deviation from 0 degrees was multiplied with the control parameters and lastly, the driving signal on the signal generator was updated[92]. Schematics for PLL and measurement circuitry are illustrated in Figure 2.6. Parts that are controlled through LabVIEW software were depicted within yellow box.

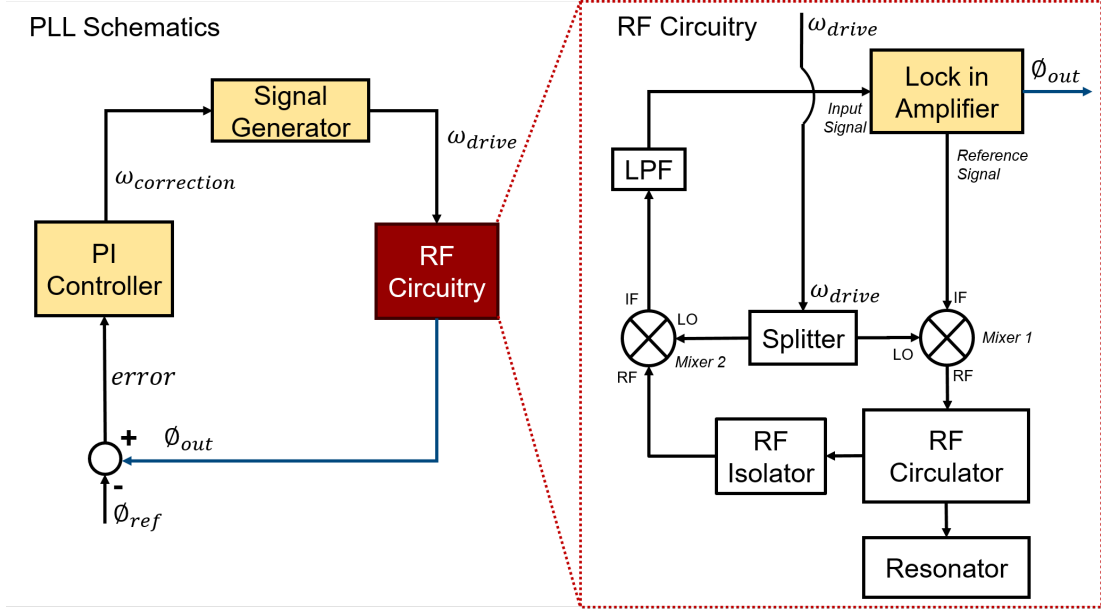


Figure 2.6: Measurement circuitry

At this point, it is important to elaborate on the noise level in the measurement system. Noise in the measurement system is expressed by Allan Deviation which is defined as instability of the frequency over a time period [93]. It is formulated as in Equation 2.1:

$$\sigma_y(\tau) = \sqrt{\frac{1}{2\tau^2} \langle (x_{n+2} - 2x_{n+1} + x_n)^2 \rangle} \quad (2.1)$$

Here, τ is the observation time. For our measurement setup, it also determines the minimum resolvable frequency shift. The resonance frequency of 2 GHz with Allan Deviation 1×10^{-8} , by simply multiplying two values, corresponds to the minimum resolvable frequency of 20 Hz. Therefore, Allan Deviation should be as small as possible for a sensitive measurement. Typically, Allan Deviation was around $1 - 4 \times 10^{-8}$, and the best Allan Deviation value achieved with these devices and the circuitry was 5×10^{-9} with PLL time of 400 ms.

2.3.2 Cell Culturing

Human breast cancer cell line MDA-MB-231 was purchased from ATCC (Manassas, VA, USA). It was labeled with a green fluorescent protein (GFP). Cells were cultured in Dulbecco’s modified Eagle’s medium (Biowest, Nuaille, France), supplemented with 10% filtered fetal bovine serum (FBS, Biowest), 1% non-essential amino acid (Biowest), and 50 U/ml penicillin/streptomycin (P/S, Biowest). FBS was filtered with a sterile filter having 0.22 μm pore size before it was added to DMEM. Content of the prepared DMEM solution is summarized in Table 2.1.

DMEM	P/S	NEAA	FBS
500 mL	5 mL	5 mL	50 mL

Table 2.1: Content of the DMEM solution

The presence of mycoplasma in cells was tested regularly using MycoAlert Mycoplasma Detection Kit (Lonza, NJ, USA). The cells were incubated at 37°C incubator (Thermo Scientific, IL, USA) under a humidified atmosphere of 5% CO₂. For the experiments, cells were trypsinized (Biowest) and collected with a growth medium as a cell suspension. They were then counted and typically 90,000 – 500,000 cells/mL solution was prepared for experiments.

Cells were cultured in 4 different culture plates: 35 - 100 - 150 mm culture dish & 6 well culture plate. In Figure 2.7, details of the amount of buffer used for maintaining cell culture are provided. Cells were kept within the incubator (Thermo Scientific - Steri Cycle i160) and their medium is changed regularly, dead cells were washed with PBS (Biowest - Dulbecco’s Phosphate Buffered Saline). Cells were passaged and cultured in the new plates inside the Biosafety Level 2 culture cabinet (Thermo Scientific Safe 2020). For the experiments, cells were cleaned up and passaged using Trypsin (Biowest - EDTA 10x), and to cease the toxic effect of Trypsin, the medium was added to the reservoir.

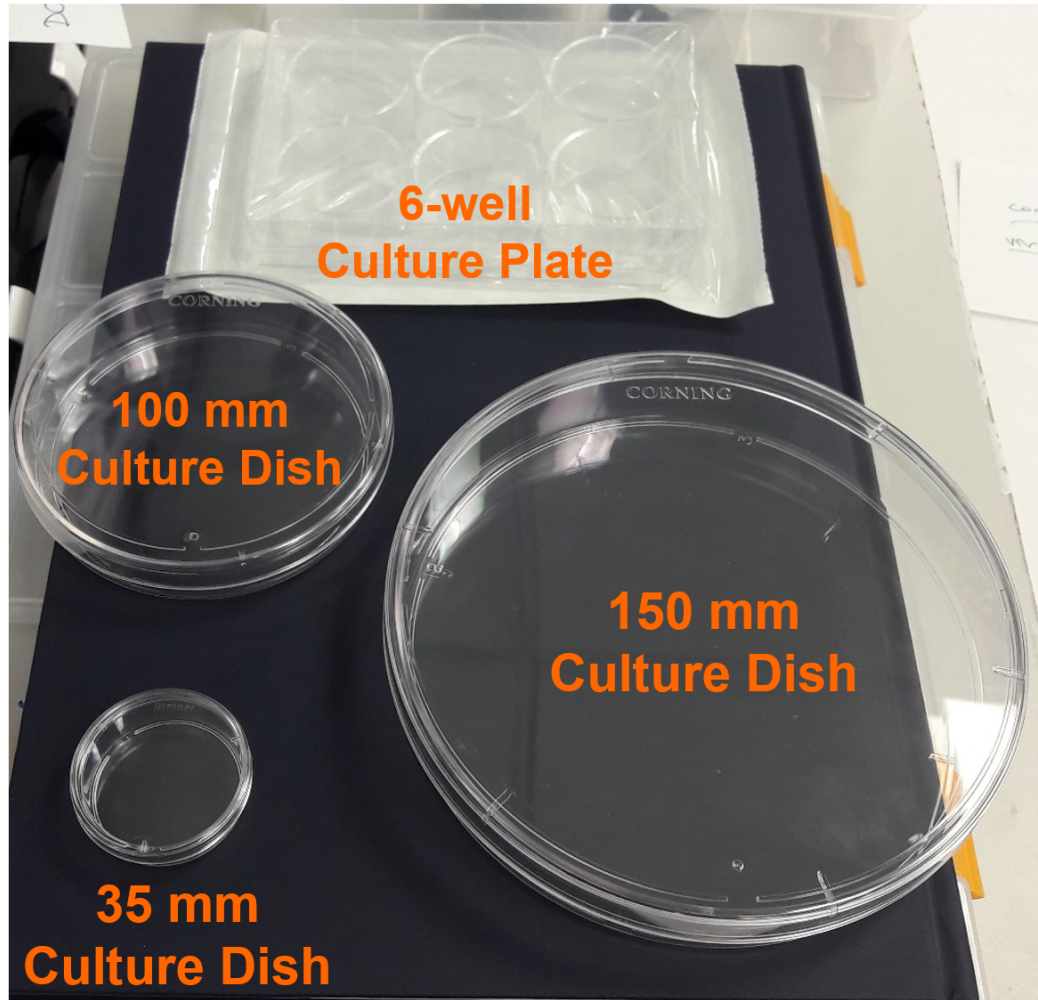


Figure 2.7: Plate sizes & buffer amounts

	DMEM	PBS	Trypsin
150 mm Culture Dish	10-12 mL	5-6 mL	2-3 mL
100 mm Culture Dish	5-6 mL	2-3 mL	1-2 mL
35 mm Culture Dish	1 mL	1 mL	0.5 mL
6 Well Culture Plate	1 mL	1 mL	0.5 mL

Table 2.2: Buffer amounts according to the plate size

2.3.2.1 Cell Freezing Protocol

Once the cells were cultured, surplus cell lines can be frozen and stored in -80°C fridge. To freeze the cells, first cells should be passaged and put into a falcon tube. Then using a centrifuge, cells should be sedimented and they should form a pellet at the bottom of the falcon tube. Spin parameters for the centrifugation process are as follows: Temperature: 4°C , Speed: 1500 rpm, Duration: 5 minutes. Falcon tube containing cells should be balanced with another tube having a similar weight.

After the centrifugation, the medium should be disposed and a new medium with the following content: 10% DMSO, 10% filtered FBS, 80% DMEM should be prepared. This new medium is added to the falcon tube containing cell pellets and using a pipette the solution should be mixed. Then cryo vials are labeled properly (name, passage number, date) and cells in the new medium are distributed to the cryovials. Typically, 1 mL of cell solution is added to 6 different cryo vials, therefore, 6 mL of the new medium is needed to be prepared containing: 600 μL DMSO, 600 μL filtered FBS, and 4.8 mL DMEM.

2.3.2.2 Cell Defreezing Protocol

When needed, cells stored at -80°C can be de-frozen and cultured again. To do that: cryo should be taken out from the fridge and waited until the cryo melts, meanwhile 5 mL of DMEM should be added to a falcon tube. Once the cryo melts fully, cell should be added to the falcon tube having 5 mL DMEM with the pipette. Typically cryo's have 1 mL of the solution therefore 6 mL of the solution should be achieved at the end.

Then the same centrifugation process should be followed with the same parameters used in the freezing protocol. After the centrifugation, cells should remain at the bottom of the falcon tube and the medium should be disposed. Add 5-6 mL fresh medium and stir the cells with a pipette. Then, cells with the medium can be spread to the culture dish or plate.

2.4 Experimental Results

2.4.1 Size Correlation Experiments

In the first resonance mode of the resonator, the geometrical volume of a cell obtained from optical microscope images was correlated to its electrical volume which will be expressed in terms of the microwave signals. Figure 2.8 shows three consecutive frequency shifts: 0.81 kHz, 1.16 kHz and 1.27 kHz. As the amount of shift increases, the area of the corresponding cell seen under the optical microscope also widened.

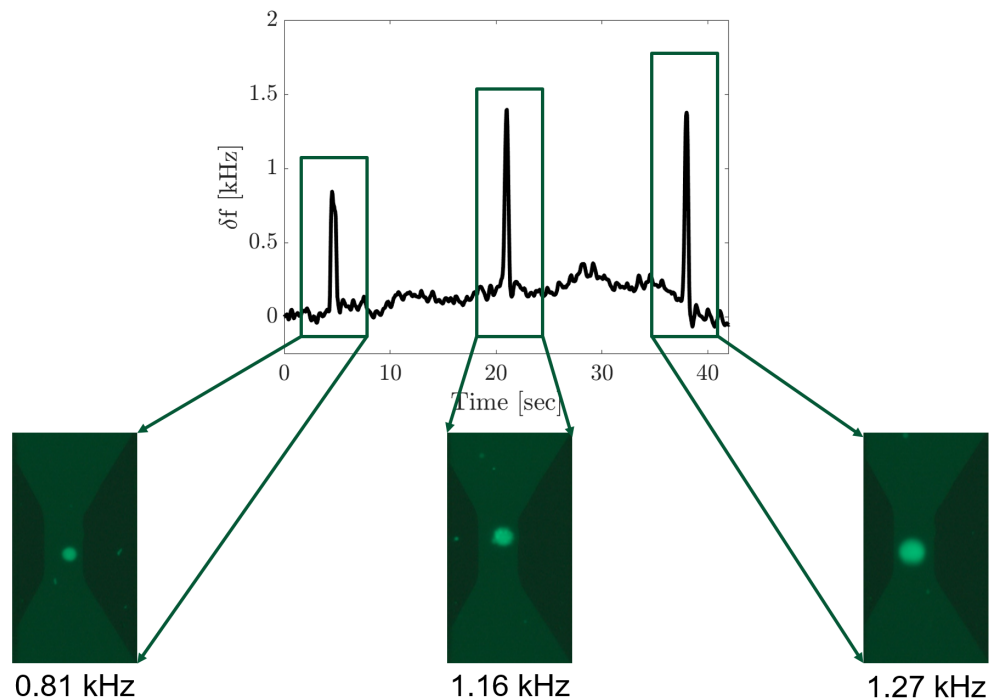


Figure 2.8: Size correlation

Optical microscope images of the cell, namely MDA-MB 231 LUC2 GFP, and electronic data were recorded simultaneously. From the bright field images, the number of pixels for each cell is calculated on MATLAB. Each measurement was carried out repetitively so that a mean and standard deviation value were

estimated. The size of a pixel was extracted from the device dimensions, with that pixelated area was converted to the actual area, and then assuming a spherical shape, it was converted to volume.

In the first experiment, the resonance frequency was tracked at 2.19 GHz with a frequency stability of 1.8×10^{-8} . After optical images were processed, the volume of each cell was matched with the frequency shift and as a result an almost linear relation was obtained as in Figure 2.9a. Some cells were larger as the cell division was seized at a certain phase, so few data points are having a large volume. In Figure 2.9b, some cells, depicted in circle in Figure 2.9a, show linear relation between volume and induced frequency shift 2.9b. The linear trend is stronger for the cells passing in between two sensing electrodes (red data points in Figure 2.9a), however, as the cells pass through electrodes (blue data points in Figure 2.9a), dispersion increases. The root mean square value for the goodness of fitting is 0.1 kHz for the nonoverlapping cells, 0.44 kHz for the overlapping cells and the overall dispersion value is 0.26 kHz.

PLL time, that is the time passing when phase re-locks to zero degrees under a given offset, is 500 ms. In the analysis, cells passing faster than the PLL time are extracted as data for both microwave and size in optical microscopy were less reliable. Sensitivity of the sensor in Figure 2.9a is on average $0.33 \text{ Hz}/\mu\text{m}^3$. For a given Allan Deviation and resonance frequency value, the minimum resolvable volume is around $180 \mu\text{m}^3$. This resolution corresponds to a minimum detectable difference of 150 nm in the cell radius for a cell having 10 μm radius.

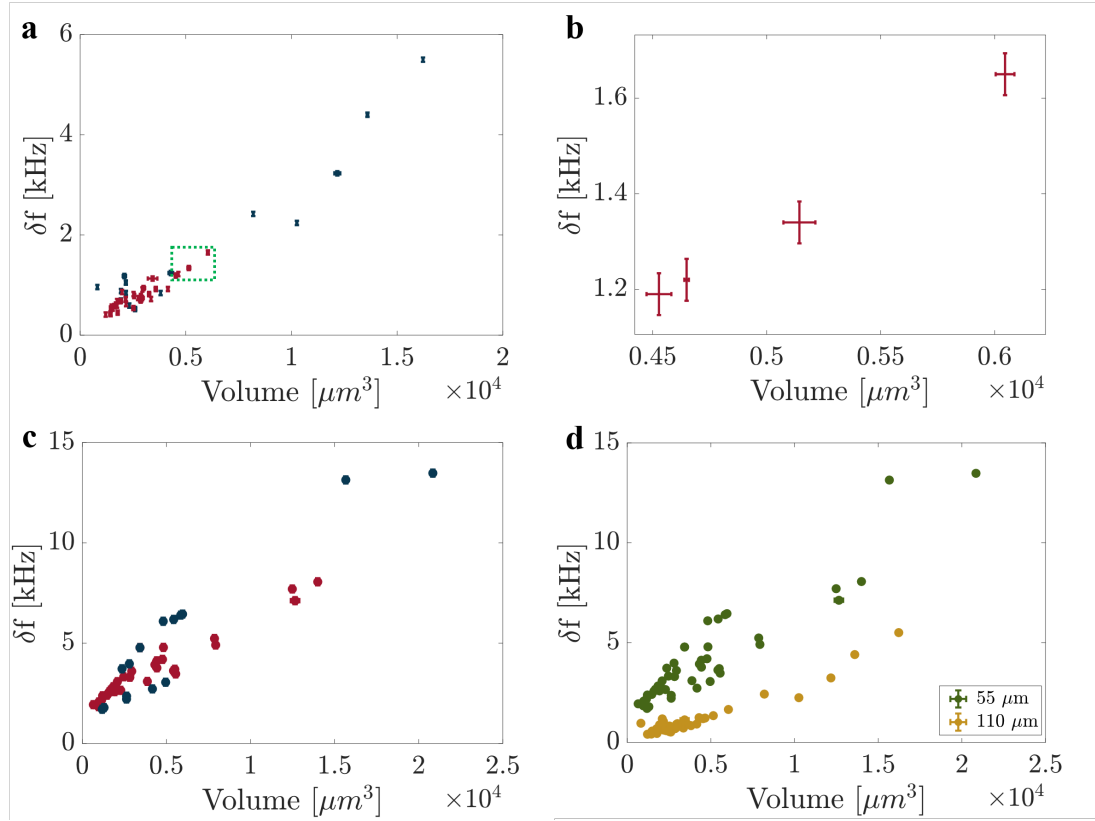


Figure 2.9: Size correlation experiments

In the first experiment height of the microfluidic channel was $110\ \mu\text{m}$, to see the effect of the channel height, another device was fabricated with channel height of $55\ \mu\text{m}$ and the first resonance mode of this new device was at $2.72\ \text{GHz}$. The same experimental procedure was followed and a similar linear relation was obtained as in Figure 2.9c. The dispersion value for non-overlapping cells is $0.43\ \text{kHz}$ and for overlapping cells, its $1.23\ \text{kHz}$, overall dispersion is $0.92\ \text{kHz}$. The sensitivity of this device on average was $1.2\ \text{Hz}/\mu\text{m}^3$.

When the results of the two experiments were plotted on the same graph (Figure 2.9d), it is obvious that frequency shifts increase when cells pass closer to the sensing electrodes.

2.4.2 Calibration Experiments with Microparticles

In the next step, in order to elucidate the positional dependency in the lateral direction, standard-sized 20 μm micro-particles (Sigma, Supelco - 74491) were used. The original solution was diluted with deionized water at a ratio of 40:1. Using another device with a resonance frequency of 2.52 GHz, the same experimental procedure was repeated as with the cells and recorded the frequency shifts at different points along the sensing region. Each particle was trapped near the sensing region and repeatedly moved it back and forth several times along the transition location by reversing the direction of the applied pressure with respect to the reservoir. While the pressure was reversed, no significant change in the horizontal position of the trapped particle was observed.

To obtain the trend line, statistics of different particles were obtained, each of which transited at a different position along the sensing region. The positional sensitivity is shown in Figure 2.10a by partitioning the sensing region into eleven different subsections – along the most densely visited trajectories of the particle flow for each experiment.

In Figure 2.10, the blue data points indicate a vertical transition path along the sensing electrodes, the red data points are for the particles passing in between two electrodes without any overlap, and the green data points are when a fraction of the particle overlaps with the top of the signal or ground electrode. The shift in the resonance frequency turns out to be larger near the edge of the ground electrode. The frequency responsivity is reduced by more than half over the signal electrode. However, the responsivity at the center of the sensor, where there is no overlap with the electrodes, is almost constant within the noise level (Figure 2.10). This result indicates that microwave measurements can be used for size measurements, without any need for additional microscopy for position determination, as long as the particle flow is confined between the electrodes which can be achieved by minor changes in the design.

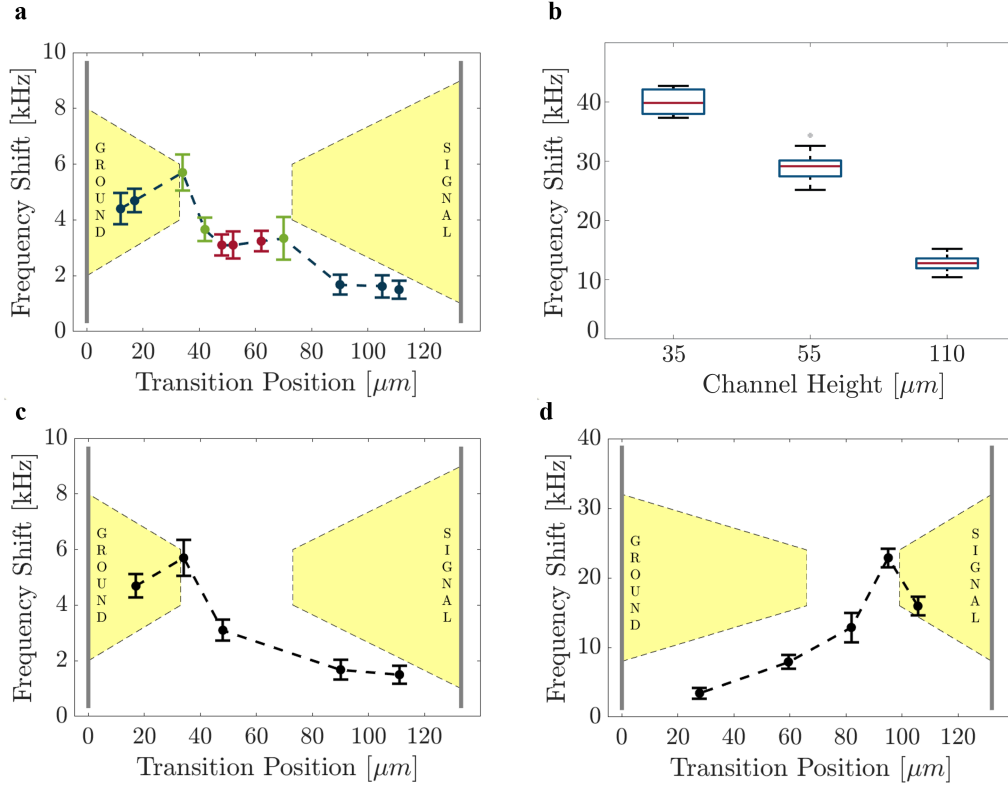


Figure 2.10: Positional dependence

Standard-sized particles were also used to investigate the effect of channel height for the particular case. The particle was trapped in between the electrodes for different channel heights: 35 μm , 55 μm , 110 μm . From Figure 2.10b, as the channel height increases, that means the particle is potentially further away from the sensing electrodes, the amount of frequency shifts recorded decreases. However, as the channel height was reduced, due to increased channel resistance and clusters, the control of the particles becomes stringent.

Then the behavior obtained in Figure 2.10a was elaborated more and a sensor that had a reversed PDMS alignment was fabricated with same channel height. In other words, this time ground electrode remained more within the channel. Similar transition positions were spanned as in the case of Figure 2.10c and the trend in frequency modulations was also reversed (Figure 2.10c-d).

2.4.3 Single Cell Trapping

After standard-sized micro-particle experiments were performed, using the same device single-cell trapping experiments were conducted. By fine-tuning the applied pressure dynamically, a single cell was trapped and made to pass back and forth between the sensing electrodes. Fluorescent optical images of the same cell were processed through a custom-built image processing algorithm. The algorithm counts the number of white pixels corresponding to the geometrical size of the cell and calculates the area of the fluorescent cell by considering 20 consecutive frames as in Figure 2.11. Through the algorithm, the transition position, dwelling time, and velocity of the cell can also be obtained. A detailed schematics for the image processing algorithm is provided in the appendix section (Appendix A, Figure A.3).

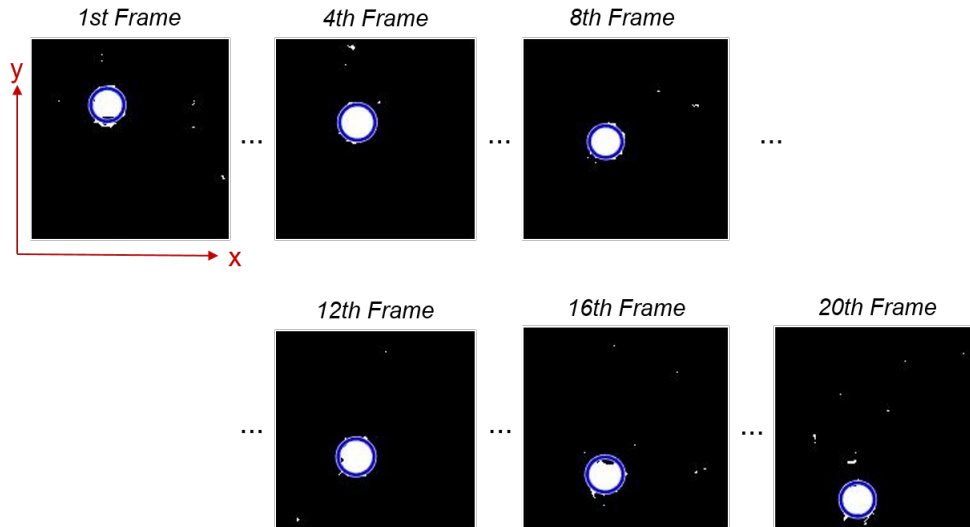


Figure 2.11: Image processing algorithm

While data were recorded for 30 minutes, the applied pressure with respect to the reservoir was continuously changed and the target cell made several passes from the sensing electrodes. The mean value for the frequency shifts turned out to be 4.67 kHz (for a 2.515 GHz resonance frequency) with a standard deviation of 0.63 kHz (Figure 2.12a). In the beginning, the cell was trapped toward the signal electrode, and by time, the cell skidded toward the ground electrode due

to fluctuations in the applied pressure. During the relocation, the amount of the shift increases as expected by the increasing sensitivity of the sensor on the ground electrode and maintains the same trend until the end of the experiment (Figure 2.12b). From here, positional dependence as in the case with microparticle experiments was reaffirmed.

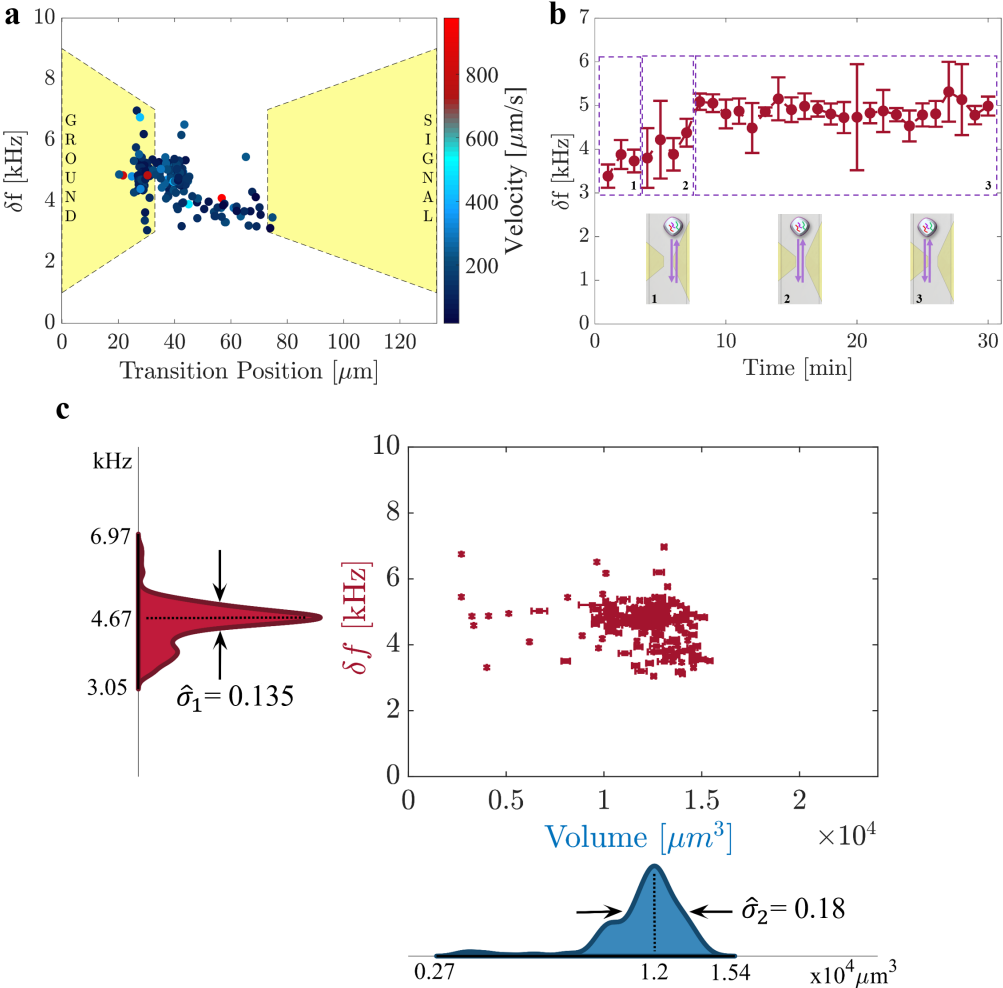


Figure 2.12: Single cell trapping

The size of the trapped cell was estimated by an image processing algorithm and compared with the frequency shift statistics. It is expected the algorithm to yield close volume values as the same cell is processed in different frames. In fact, Figure 2.12c illustrates the volume concentrated to approximately 1.2×10^4

μm^3 which can be seen at the bottom histogram as well in Figure 2.12. Both histograms have certain peaks in the size distribution just below the average of the mean value.

2.4.4 DMSO Experiments

After it has been shown that single cells can be trapped and their frequency shift statistics can be achieved, another experiment was designed to detect the biophysical change of a single cell. Using a new device, resonance frequency was tracked at 2.72 GHz with frequency stability of 1×10^{-8} .

Dimethyl sulfoxide (DMSO, ChemCruz), a chemical that accelerates dehydration, was added to assess the change in the size of the cells [94]. The effect of DMSO was optimal when pretreating the cells within a large reservoir for approximately half an hour. Then, pretreated cells were transferred to the microchannel, and a target cell was selected and trapped around the sensing region. Then, the applied pressure was reversed dynamically, and the electronic data were recorded.

As DMSO causes contraction of the water lipid interfacial region [95], shrinkage in the lipid bilayer of the cells was expected to be observed which causes decreases in the volume of the cell. Cells were treated with DMSO in a large reservoir and transferred to the microchannel. Ten points moving average was used and it was observed that the average of frequency shifts decreased from 6.43 kHz to 4.64 kHz within half an hour (Figure 2.13a). Similarly, using the same device, a control run was also recorded with DMEM and cells were treated for 15 minutes. After 30 minutes, the change in the average frequency shift was only 350 Hz which is close to the noise level (Figure 2.13b).

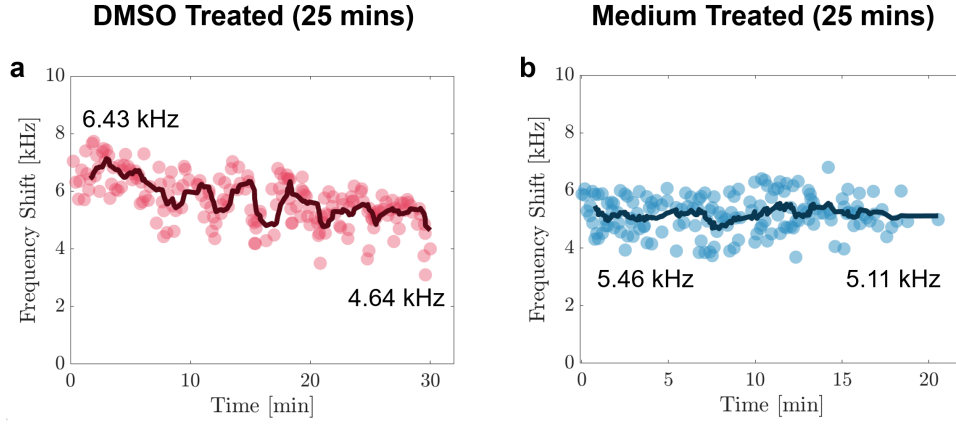


Figure 2.13: DMSO experiments

With this experiment, Microfluidics Integrated Microwave Sensors (MIMS) can be proposed as a physical sensor that can sense morphological changes of a single cell in real-time. With further investigation and optimizations, drug response/resistance of a single cell can be observed using MIMS.

2.5 Analytical Calculations for Frequency Shifts

Resonant microwave sensors can be modeled as RLC systems as depicted in Equation 2.2. This formulation is analogous to NEMS which can be modeled as a mass-spring-dashpot system.

$$f_0 = \frac{1}{2\pi\sqrt{LC}} \quad (2.2)$$

In the proposed microwave sensor, the sensing was based on permittivity difference between cell and fluid which modulates the capacitance of the overall system. This can be formulated as in Equation 2.3

$$\frac{\Delta f}{f_0} = -\frac{1}{2} \frac{\Delta C}{C} \quad (2.3)$$

Capacitance change can be calculated by the Equation 2.4 provided by Ferrier et al. [28] .

$$\Delta C = 4\pi\epsilon_{fluid} \left(\frac{E_{rms}^2(r_{cell})}{U_{rms}^2} \right) r^3 K_{cm} \quad (2.4)$$

where r is the radius of the cell, U_{rms} is the applied voltage, K_{cm} is the Clausius-Mossotti factor that is a function of permittivity of fluid and cell (Equation 2.5).

$$K_{cm} = \frac{\epsilon_{cell} - \epsilon_{fluid}}{\epsilon_{cell} + 2\epsilon_{fluid}} \quad (2.5)$$

Capacitance for the overall sensor was calculated by taking the volume integral as in Equation 2.6.

$$C_{eff} = \frac{\epsilon_{eff}}{U_{rms}^2} \int E_{rms}^2 dV \quad (2.6)$$

Here ϵ_{eff} is the effective permittivity of whole sensor, i.e. microfluidic channel & fused silica chip. Effective capacitance of the sensor is formulated as follows:

$$C_{eff} = \alpha \epsilon_{eff} \frac{E_{rms}^2(r_{cell})}{U_{rms}^2} V_{sensor} \quad (2.7)$$

where V_{sensor} is the entire volume of the chip and α is called the enhancement factor, i.e. ratio of the normal gap which is $400 \mu\text{m}$ for this design to the sensing gap which is $50 \mu\text{m}$. Therefore, the enhancement factor for the proposed design is 8.

Using Equation 2.4 & Equation 2.7, capacitance ratio can be rewritten as in Equation 2.8:

$$\frac{\Delta C}{C_{eff}} = \frac{\alpha \epsilon_{fluid}}{3 \epsilon_{eff}} K_{cm} \frac{V_{cell}}{V_{sensor}} \quad (2.8)$$

The volume of the sensor was calculated by signal length, the gap between signal - ground, and height of the channel. Here, the full height of the channel (100 μm) is considered as it is the maximum distance for detection. The volume ratio of cells having 10 μm radius to sensor turns out to be around 1.54×10^{-6} .

Taking relative permittivity of cell as 50 [96] and considering effective permittivity of sensor as 42 which is the average of water and fused silica ($\epsilon_{water} = 80$ & $\epsilon_{silica} = 4$), ratio of the permittivity values turns out to be ≈ 2 and $K_{cm} = -0.143$. Inserting all these values into Equation 2.8, the capacitance ratio turns out to be -1.12×10^{-6} . From here, the frequency ratio turns out 5.58×10^{-7} .

$$\frac{\Delta f}{f_0} = 5.58 \times 10^{-7} \quad (2.9)$$

For a resonance frequency, f_0 , around 2.19 GHz as in Figure 2.9a, the frequency shift is estimated to be in the order of a few kHz.

$$\Delta f \approx 1.22 \text{ kHz} \quad (2.10)$$

In the estimation, the same parameters in Figure 2.9a were used. As a next step, cell radius 3 μm to 20 μm was spanned with an increment of 1 μm and illustrated with yellow data points in Figure 2.14. Uncertainty in the shift was calculated with the experimental values and corresponds to the noise level of the measurement. Deviation in the cell size was estimated with minimum resolvable change in the radius which was 150 nm for the experiment as explained in the size correlation part. Estimated values are in concordance with the experimental data.

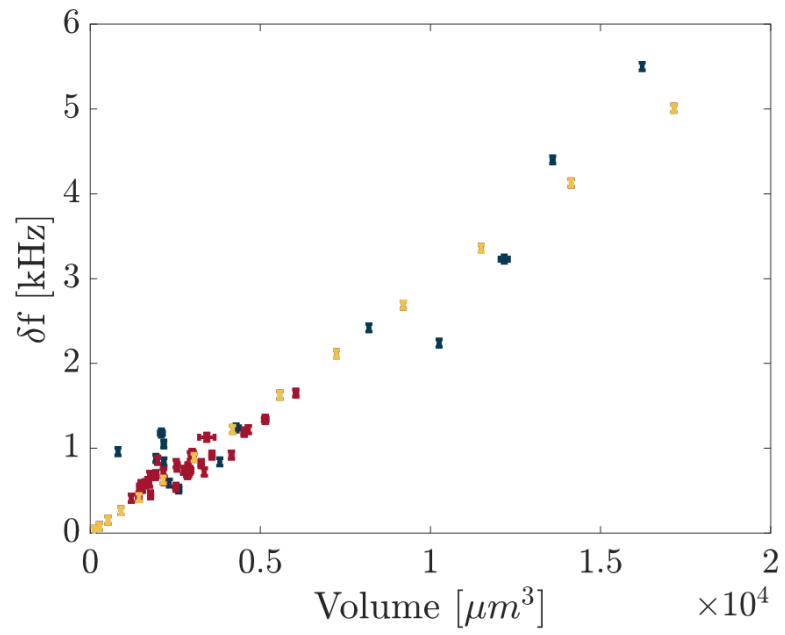


Figure 2.14: Shift estimation on experimental data

Chapter 3

Nanomechanical Flow Rate Sensor

In the second application of the bow tie shaped CPW microwave resonator, a novel approach to flow rate sensor will be envisaged. Most of the commercial flow rate sensors work based on hot wire anemometer. One of the well-known technology is Sensirion's CMOSens. In this case, the flow rate is measured by considering the heat dissipation profile at two different locations. Herein, a flow rate sensor based on nanomechanics & microwave will be envisioned. In nanomechanics, the effects of fluids in nanomechanical systems have been investigated broadly, however, in most of these studies, the fluid played the secondary role, for instance, in suspended microchannel resonators fluid causes damping which reduces the quality factor of the resonator [5].

Using the same microwave design explained in Chapter 2, an exquisite sensing mechanism was patterned on a membrane with wrinkles and when the flow is on bistable states are observed on wrinkles. These flow-induced states, to our knowledge, are the first time used as a flow rate sensor. The formation rate of these bistable states depends on the effective flow rate, i.e. higher the flow rate, the more frequently those states are observed.

All operations are implemented on-chip which is crucial for the ventilation machines widely used during the COVID-19 pandemic, drug delivery, organ-on-a-chip, and droplet generation applications. What is measured by a commercial flow rate sensor might be different from the actual flow rate which impairs the precise delivery of oxygen level, amount of the drug & nutrients for the target application.

3.1 Device Fabrication

In the previous chapter, to detect single cells, bow tie CPW was patterned on a fused silica wafer. However, for the flow rate sensor, Silicon(*Si*) substrate that is 500 μm thick was used. 2.2 μm oxide layer(*SiO₂*) was sandwiched between Si substrate at the core and 220 nm thick Silicon Nitride (*Si₃N₄*) at the outer layer. Figure 3.1a illustrates layers of the used wafer (not scale).

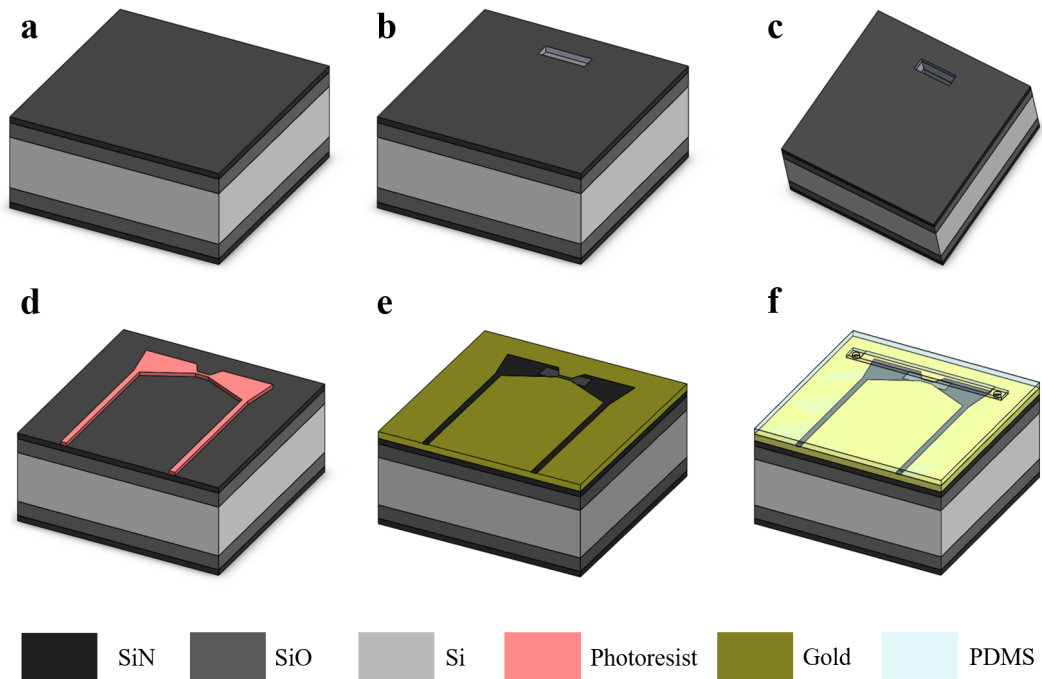


Figure 3.1: Fabrication steps of the flow rate sensor

As a first step, a window for the membrane formation was masked with the desired dimensions and exposed to the UV light with photolithography. For this application, the size of the membrane is quite large (order of mm) to increase the wrinkle formation.

From the bottom of the wafer 220 nm thick nitride layer was anisotropically etched (Figure 3.1b) using Inductively Coupled Plasma (ICP) with the following etching recipe: Gases: CF_4 : 20 sccm, CHF_3 : 3 sccm; Coil Power: 400 Watt, Platen Power: 100 Watt, Duration: 5 minutes. Unless the color change was observed at the end of 5 minutes, the same recipe was repeated for additional 1-2 minutes. Once nitride was successfully etched, the color of the target region changes from grey to pink which means the oxide layer is unveiled.

When the nitride at the bottom was etched, the nitride layer at the top could be suspended to form a membrane through wet etching of SiO_2 & Si (Figure 3.1c). KOH solution is composed of 100 gr of KOH & 300 mL DI water. KOH should be added slowly and with a stirrer and it should be mixed slowly to forestall splashing. The wafer was left within the KOH solution for 24 - 48 hours, and checked every 12 hours. Once the membrane was formed, the chip was ascended from KOH solution and dipped into DI water to get rid of KOH residues. The most critical step is after that: the liquid inside the pyramid (membrane window) should be absorbed with a tissue slowly and gently, otherwise, such a large membrane explodes. Pressurized nitrogen or air should not be used to dry out the chip.

In the next step, the top of the chip was coated photoresist (AZ5214) with the following spin parameters: Speed: 1000 rpm, Time: 20 seconds, Acceleration: 200 rpm. Then, the microwave design was patterned using photolithography and the sensing electrodes were aligned on the membrane (Figure 3.1d). Then, UV exposed chip was coated with 10 nm Chromium and 100 nm Gold, using thermal evaporation and left for the overnight lift-off (Figure 3.1e).

In the last step, the soft lithography process for the PDMS microchannel fabrication was performed by following a similar procedure with the same parameters

explained in Chapter 2.2. The fabricated chip and PDMS microchannel were plasma-activated and under a microscope microfluidic channel was aligned on both sensing electrodes & the membrane (Figure 3.1f).

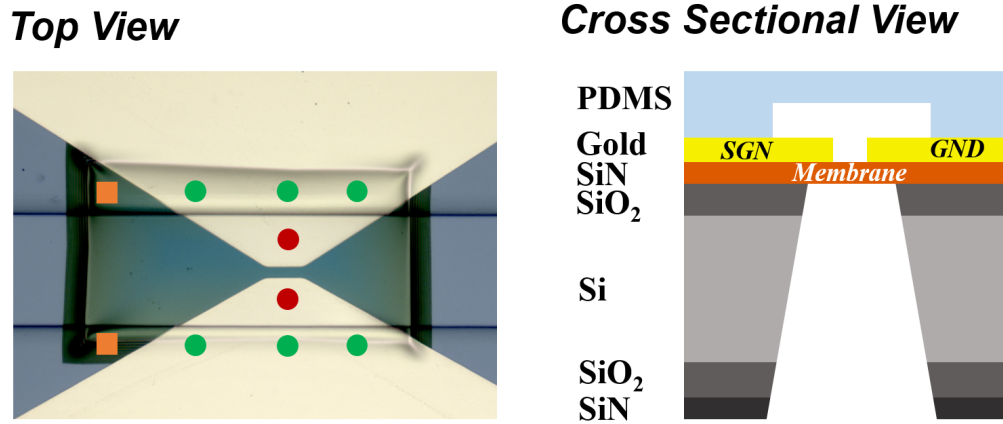


Figure 3.2: Layers of flow rate sensor

The top & side view of the final sensor is illustrated in Figure 3.2. In the Top View: red dots are the points where the membrane was clamped by only electrodes; green dots are the points where the membrane was clamped both by electrodes & PDMS; orange squares are the points where the membrane was clamped by only PDMS.

3.2 Experimental Setup

Experimental Setup used for the proposed flow rate sensor is so similar to the setup described in Chapter 2.3. However, this time there is a reference flow rate sensor (Fluigent FRP) which is critical for comparing proposed sensor performance. The reference sensor works based on hot wire anemometer and it can measure up to $120 \mu\text{L}/\text{min}$ (calibrated with DI water) within a glass capillary having $430 \mu\text{m}$ inner diameter. The flow was driven by a pressure controller (Fluigent MFCS) instead of a syringe pump that can could alter the frequency

response of the resonator. However, a stable pressure controller response of the resonator was isolated from the pressure source.

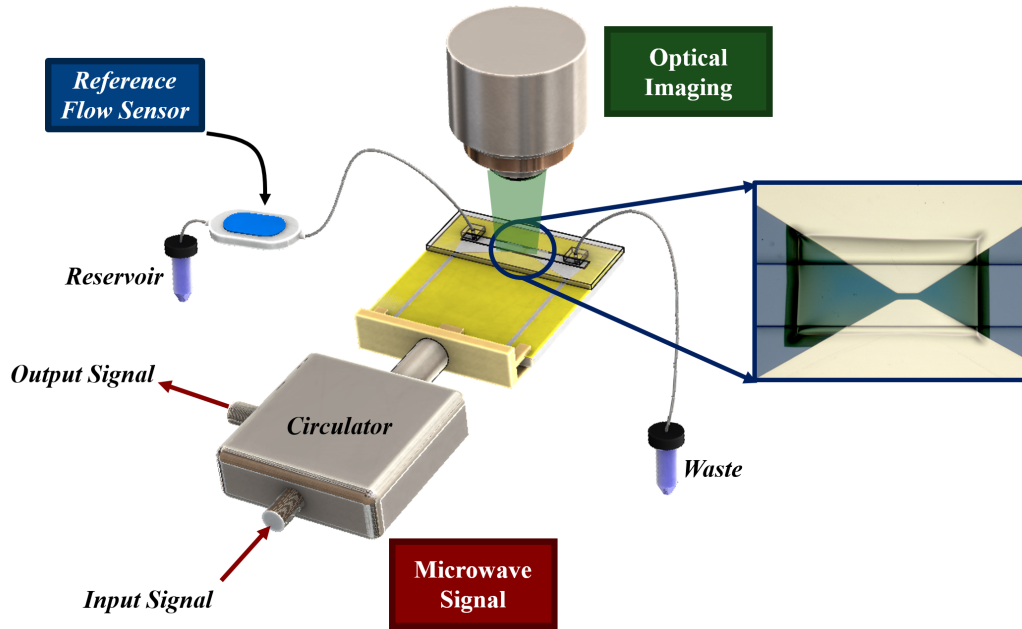


Figure 3.3: Experimental setup

Similar to the previous chapter, the chip was placed under microscope and the required electronic connections were made. The same circuitry explained in Chapter 2.3.1 was employed for microwave measurements.

3.3 Experimental Results

Once the experiment has started and the flow was on, the membrane was buckled and wrinkles on the membrane constantly cycled within the 3 different states. When the flow rate was changed, the period of these state transitions also changed. Therefore, the flow-induced instability can be utilized to determine the effective flow rate.

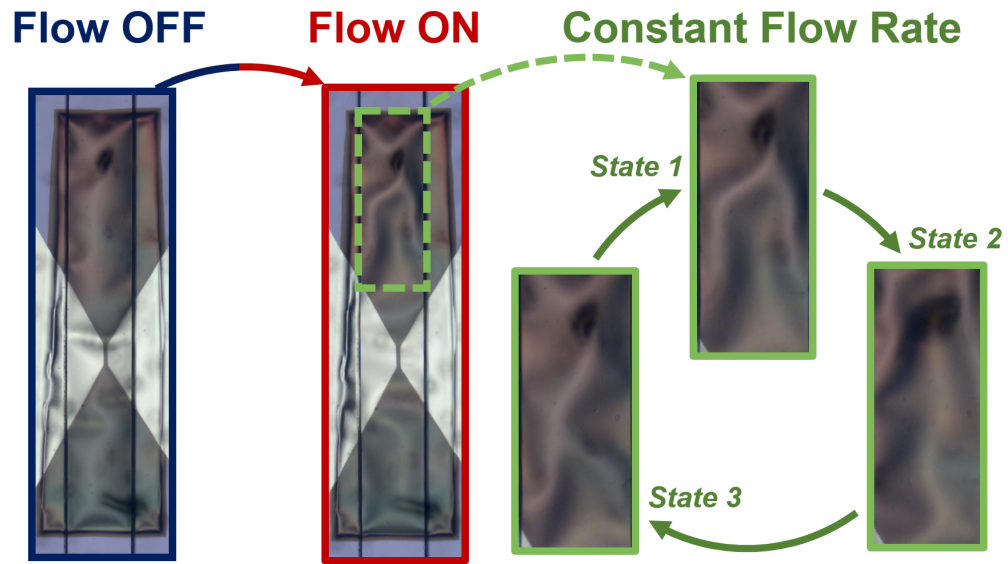


Figure 3.4: State transitions

Optical microscopy clearly showed cyclic deformation of the membrane. The membrane illustrated in Figure 3.4 had dimensions of 1.5 mm x 0.3 mm with 220 nm thickness. The period of the transitions between the states and pulsation periods matched one another.

Simultaneously, the microwave response of the sensor was recorded together with the flow rate read by the commercial flow sensor. An example of flow-induced modulation is illustrated in Figure 3.5. The figure shows the relation between the phase response of the resonator and the effective flow rate. Two different flow rates, 10 and 5 $\mu\text{L}/\text{min}$, were shown as an example: for each flow rate, the time between two consecutive pulses, named as pulse interval (T_i), remained constant. As the flow rate decreased, it was observed that the pulse intervals dilated. When the flow rate was set to 10 $\mu\text{L}/\text{min}$, pulse interval T_1 was approximately 7 seconds, whereas at a 5 $\mu\text{L}/\text{min}$ flow rate, pulse interval T_2 increased to approximately 14 seconds (Figure 3.5a).

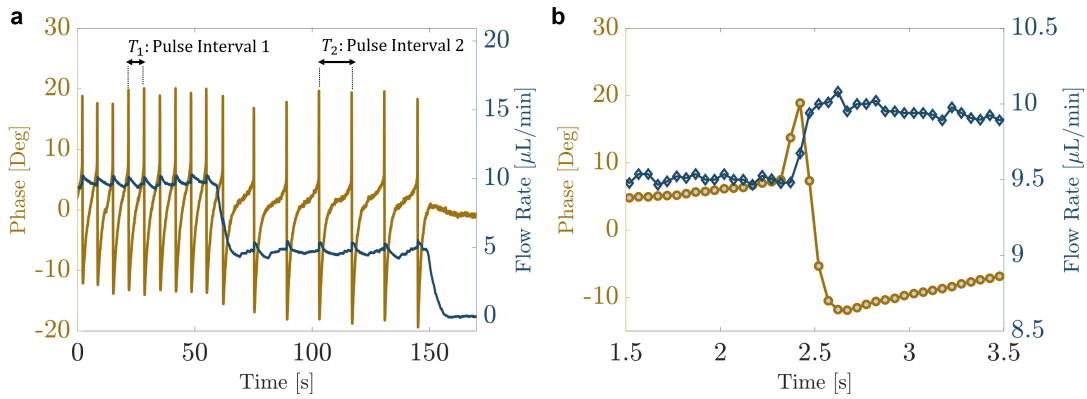


Figure 3.5: Microwave response of the flow rate sensor

Another important observation was that first resonance frequency of the resonator was modulated, then, a small perturbation in the commercial sensor was observed (Figure 3.5b). The deformations of the membrane altered the distance between electrodes at the micro level which results in the resonance modulation of the overall sensor. The sudden peaks in the flow rate that occurred right after the pulsation also supported this hypothesis since a deflected membrane resulted in an enlarged channel, which then reduced the channel resistance and caused an increase in the flow rate driven under constant pressure conditions. The perturbation of the fluid flow by the action of the sensor constitutes one limitation for this specific application; however, the design space, in terms of the composition and geometry of the membrane, is still open to striking a balance between the sensitivity and back action.

To give more insight, a full spectrum of the PLL sweep was illustrated in Figure 3.6. Pulse intervals in the resonance become more distinguishable.

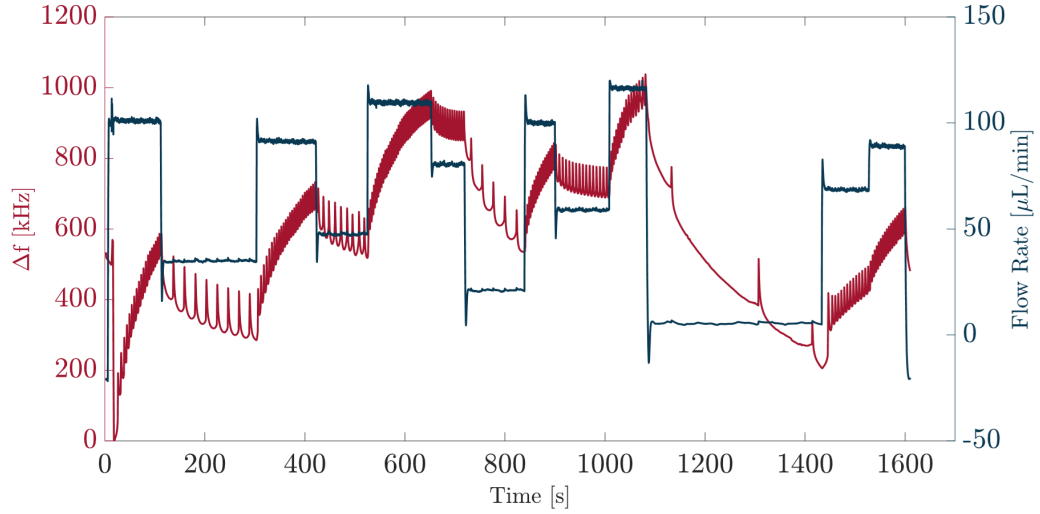


Figure 3.6: Full spectrum of the microwave response

With this further evidence, it can be concluded that the pulsations were originated from the microscale deformation of the wrinkles on the membrane. Hence, it can be proposed that a nanomembrane integrated microwave sensor (NIMS) can be used for flow rate measurements integrated on-chip. At this point, it is important to re-emphasize that these pulsations cannot be sourced from a syringe pump as no syringe pump was integrated into the experimental setup.

3.3.1 First Sensing Mechanism: Pulsation Frequency

In order to reach a minimum & maximum detectable flow rate, three different devices were fabricated to observe pulsation behavior and each time, pulsations were observed. Time interval (T_i), that is the time between two consecutive pulses converted to the frequency and named as pulsation frequency in the unit of Hz.

To enhance the sensitivity of the resonator, a large membrane, illustrated in Figure 3.4, was fabricated and used to resolve the slight increments in the flow rate. The resonance frequency of the microwave sensor coupled to the first membrane was 3.66 GHz and the dimensions of the membrane were 1.5 mm ×

0.3 mm. Results obtained with this first membrane was illustrated with the blue dots in Figure 3.7.

In the first experiment, the flow rate was set to an interval of 0 - 1 $\mu\text{L}/\text{min}$ with an incremental change of 0.1 $\mu\text{L}/\text{min}$ via the reference sensor. Until 0.3 $\mu\text{L}/\text{min}$, the sensor did not register any pulsation in the resonance. In fact, the reference flow sensor, which was used to set the flow rate of the pump, does not work well at this low flow rates: for a 0.3 $\mu\text{L}/\text{min}$ set value, the error reported in the commercial flow sensor is $\pm 0.12 \mu\text{L}/\text{min}$. Therefore, the flow condition at these small values was not reliably controlled due to the limitations of the commercial sensor; however, the absence of the pulsation might also be related to a possible critical flow speed for inducing mechanical instability. After reaching a flow rate of 0.4 $\mu\text{L}/\text{min}$, the resonator began to exhibit discernible pulses. Then, the flow rate increment was changed to 0.5 $\mu\text{L}/\text{min}$ and spanned until 3.5 $\mu\text{L}/\text{min}$. All in all, an almost linear relation was observed between flow rate and pulsation frequency.

In the second device, channel width was kept constant (250 μm), however, membrane dimensions were reduced to 800 μm by 350 μm and it was used to span a higher flow rate range. Its resonance frequency was tracked at 2.36 GHz and starting from 5 $\mu\text{L}/\text{min}$ and pulses were recorded for 300 seconds at each flow rate value. Then, the current flow rate was increased with 5 $\mu\text{L}/\text{min}$ steps until reaching the flow rate of 50 $\mu\text{L}/\text{min}$. A similar trend was observed with the second device depicted with the red data points in Figure 3.7.

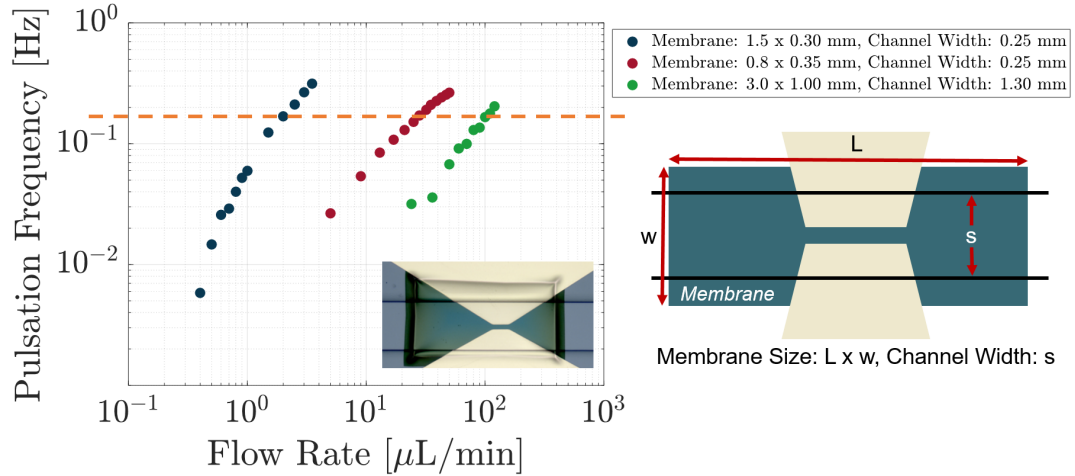


Figure 3.7: Pulsation frequency with 3 different devices

The third device was used to span until the full range of the commercial flow rate sensor ($120 \mu\text{L}/\text{min}$). The dimensions of the membrane were $3 \text{ mm} \times 1 \text{ mm}$ with a fluidic channel width of 1.3 mm . With the smallest effective pressure, the flow rate started from $24 \mu\text{L}/\text{min}$ and increased up to $120 \mu\text{L}/\text{min}$. As the flow rate increased, pulsation frequency also increased monotonically as depicted with green data points in Figure 3.7.

Figure 3.7 shows that, apart from an effective flow rate, the size of the membrane and width of the channel are also a crucial factor affecting the working mechanism of these on-chip microwave flow sensors. For instance, the orange dashed line in Figure 3.7 shows the same pulsation frequency for sensors having a different geometry. The same pulsation frequency was achieved at $2 \mu\text{L}/\text{min}$, $28 \mu\text{L}/\text{min}$, and $\approx 100 \mu\text{L}/\text{min}$ consecutively for the three sensors explained. Therefore, sensors with different geometries can be designed for different target flow ranges. Similarly, commercially available flow sensors have been manufactured according to the intended flow rate with alternating flow ranges.

After investigating the pulsation period of the phase variable of the microwave sensor, attention was turned to the shift in the resonance frequency of the microwave sensor during pulsation. The amount of frequency shift was also specific

to the effective flow rate (Figure 3.8) during pulsations. For small increments in the flow rates ($0.1 \mu\text{L}/\text{min}$), the frequency shifts do not vary remarkably (Figure 3.8a); however, for larger incremental steps, e.g. $5 \mu\text{L}/\text{min}$, a downward trend in the frequency modulations is discernible (Figure 3.8b).

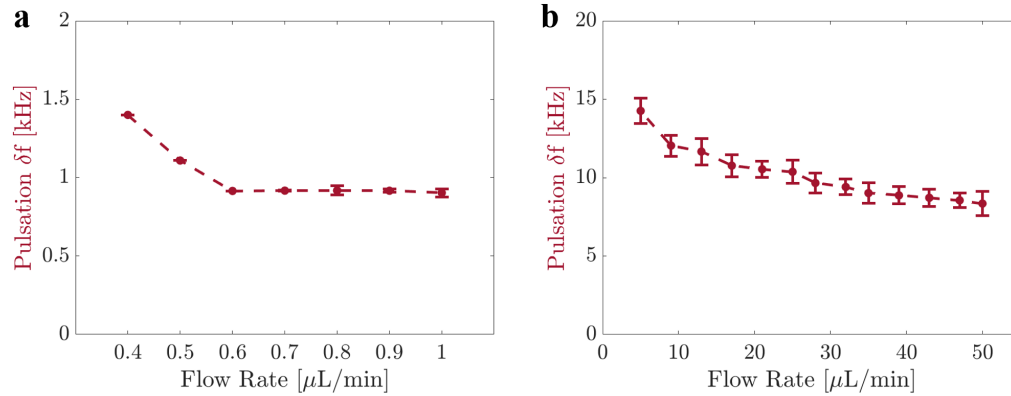


Figure 3.8: Frequency shifts during pulsations

3.3.2 Secondary Sensing Mechanism: Reset Condition

The response of the device was also investigated from the reset condition (where there was no fluid flow) to the target flow rate while driving the resonator at its resonance frequency. When the flow rate reached the target value, instant shifts in the resonance were observed. Each of these shifts depended on the magnitude of the flow rate. Therefore, the amount of frequency shift can be used as a secondary measurement method for the target flow rate.

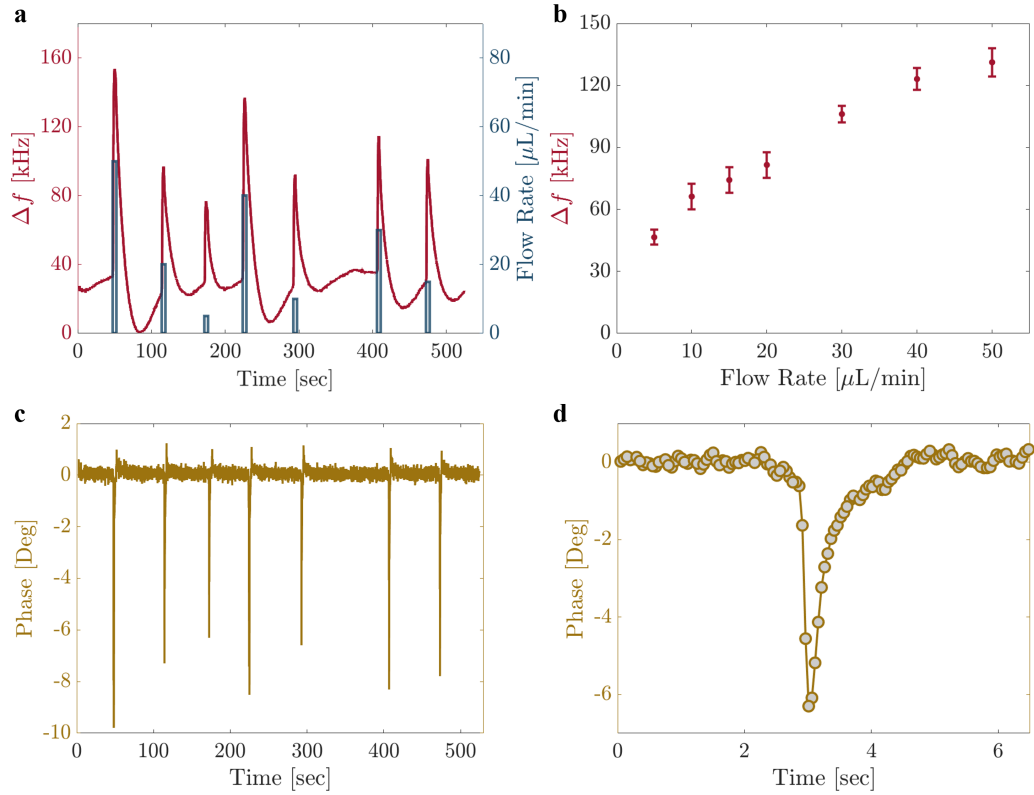


Figure 3.9: Reset condition

However, the sensitivity in this second mechanism was not as precise as that in the first mechanism (pulsation frequency). The baseline frequency fluctuations were about 1 kHz which can be extrapolated to the sensitivity level of $0.5 \mu\text{L}/\text{min}$, which is on a par with the first mechanism (Figure 3.10). However, as shown with the error bars of Figure 3.9b, repeating the experiment at the same flow rate resulted in dispersion in the frequency shifts with a standard deviation of 5.5 kHz that was larger than the baseline frequency noise.

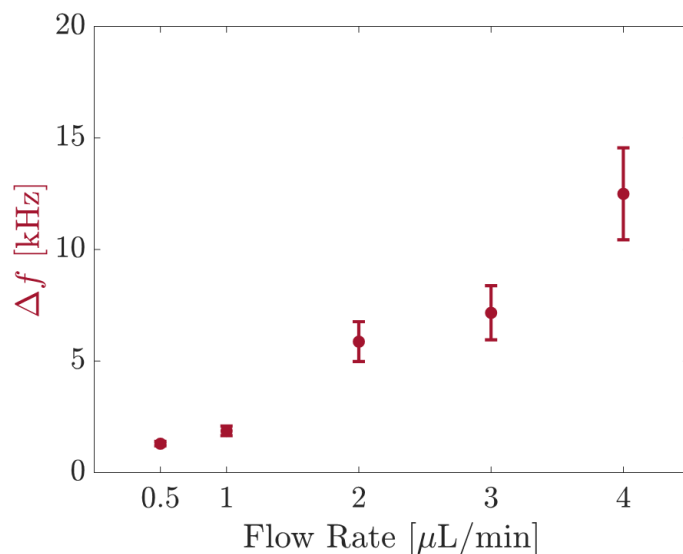


Figure 3.10: Minimum sensitivity level for the secondary mechanism

The second operation mode of the sensor was similar to a mechanism recently reported in the literature [61], which used PDMS instead of silicon nitride. However, the sensor demonstrated here exhibited a time resolution of milliseconds (Figure 3.9c-d) when the flow rate was increased step-wise. When the flow was stopped, we observed drift in the frequency that lasts for approximately 50 seconds; however, additional flow rate measurements can still be conducted during the recovery period (Figure 3.11).

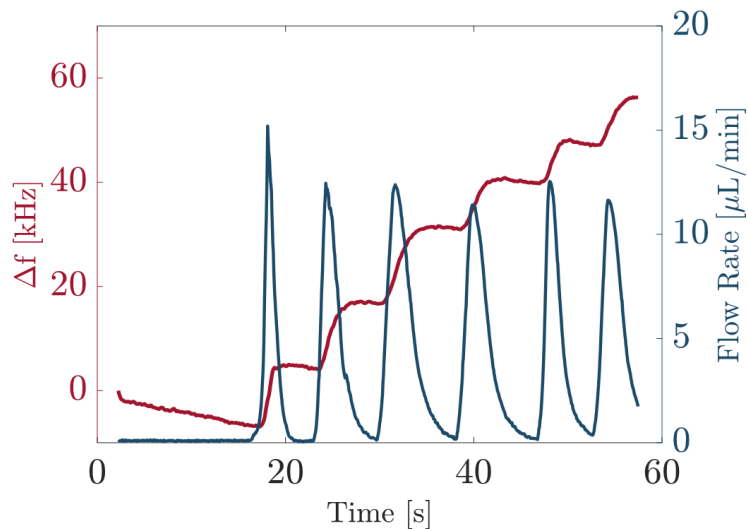


Figure 3.11: Repeatability of the secondary sensing mechanism

Average of the frequency shifts in Figure 3.11 was 10 kHz with a standard deviation of 1.5 kHz.

3.3.3 Air Flow Experiments with Secondary Mechanism

The current COVID-19 pandemic necessitated ventilation machines which are essential to keep patients alive and maintain their oxygen level stable in blood for effective treatment. For these machines, the flow sensor is the most critical component as it accurately adjusts the oxygen level. Concordantly, additional experiments have been carried on pressurizing air instead of DI water. Here, the potential of microwave resonators was shown as a flow rate sensor in the ventilation machines.

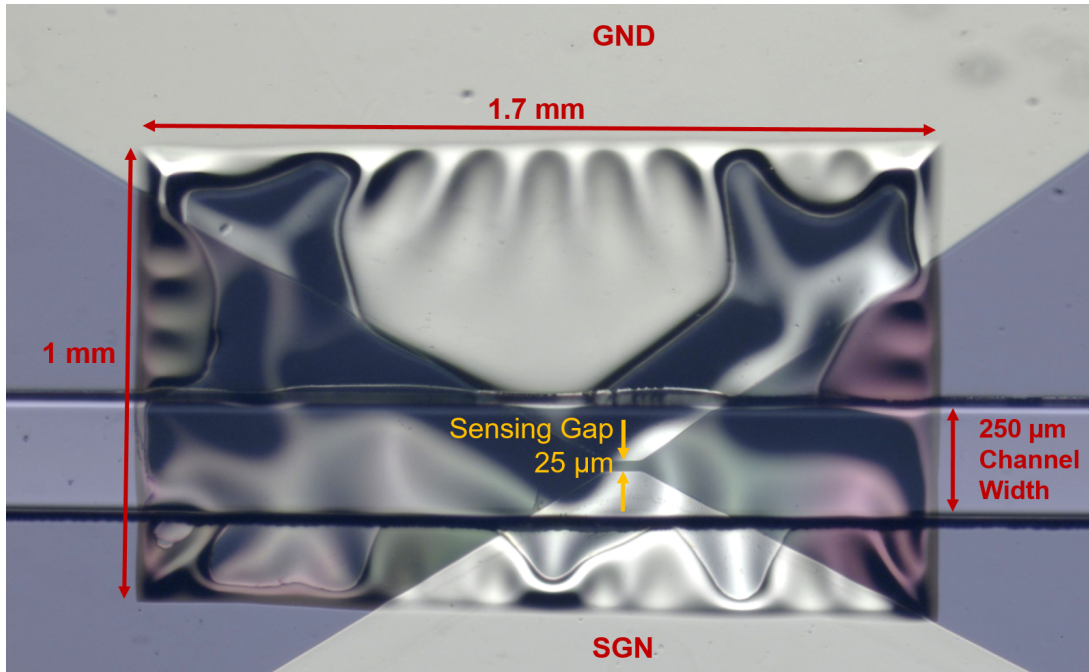


Figure 3.12: Membrane fabricated for air flow experiments

The membrane that was fabricated for this purpose has the following dimensions: 1.7 mm x 1 mm x 220 nm and two sensing electrodes were placed 25 μm apart (Figure 3.12). For airflow experiments, the third device explained in the pulsation response was also used to cover up higher flow rate values.

Since the commercial flow rate sensor cannot measure the airflow rate, a calibration process was carried to estimate the airflow rate. First, DI water was pressurized through the channel and flow rate values were recorded. Then, the flow rate values were matched with the applied pressure and overall resistance of the microfluidic components were estimated. In the resistance formula, the viscosity of the DI water was replaced with the viscosity of air and a new resistance value for air was estimated.

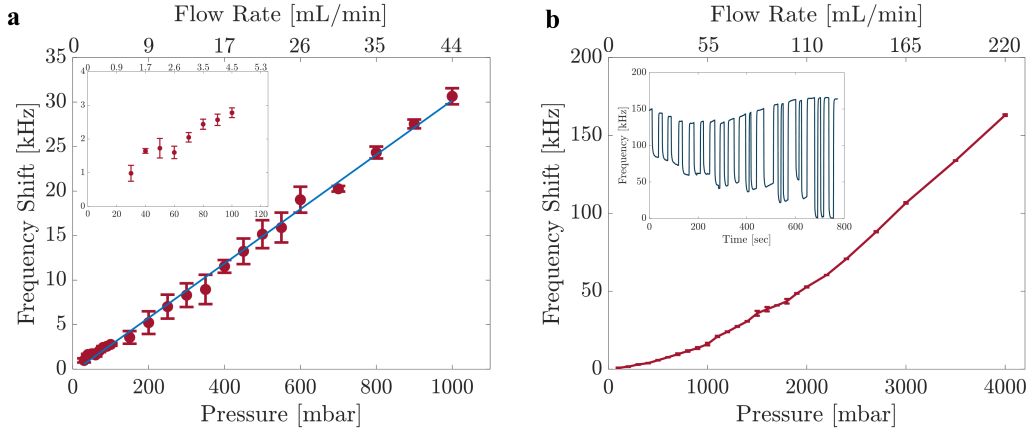


Figure 3.13: Frequency response vs Applied air pressure

In the first experiment, the device illustrated in Figure 3.12 was used and the resonance frequency was tracked at 2.54 GHz with Allan deviation of 4×10^{-8} . First, 20 mbar was applied, however, frequency response was buried in the noise. Starting from 30 mbar, frequency shifts were observed in the microwave measurement. At 30 mbar, the flow rate of the air was estimated to be 1.3 mL/min and the applied pressure was increased by 10 mbar until 100 mbar. At low flow rates, the linear relation between flow rate and frequency shift partially collapsed (Inset Figure 3.13a), however, at higher flow rates linear relation was conserved with an overall root mean squared (rms) dispersion value of 0.58 kHz (Figure 3.13a).

In the second airflow experiment, the device having the membrane dimensions of $3 \text{ mm} \times 1 \text{ mm}$ (the third device used in liquid experiments) was employed to span higher flow rates and tested durability of the low-stress nitride membrane. The pressure value started from 100 mbar and increased up to 4 bar and corresponding flow rates were estimated to be between 5 - 220 mL/min by following the same calibration procedure. As the flow rate increased, amount of the frequency shift was also increased (inset Figure 3.13b) and by spanning the full pressure spectrum a monotonic increase in the frequency response was observed and it was noted that the membrane could endure up to 4 bar (Figure 3.13b).

Chapter 4

Nanopore Sensing of Viruses

In the last application of the bow tie CPW resonator, nanoscale biological samples and particles were detected using microwave resonators. NEMS technology has already been used to detect molecules such as gold nanoparticles [97] or single proteins [98, 99]. By transferring the analytes either by Electro Spray Ionization (ESI) [16] or Matrix-Assisted Laser Desorption Ionization (MALDI) [97], the particle landed on the mechanical beam modulates the resonance of the NEMS. The amount of the shift gave spatial and inertial information about the analyte landed on the NEMS [100, 101]. Similarly, as explained earlier with the cells, nanopore integrated microwave resonators can be utilized to detect such analytes. Herein, the experiments were tested using the gold nanoparticles, polystyrene nanoparticles, and viruses. With further investigation and optimization, microwave integrated nanopore technology can pave the way to a novel biophysical sensor that can be used to characterize single viruses such as SARS-CoV-2.

4.1 Device Fabrication

Fabrication of the chip was similar to Chapter 3 and the same wafer used for the flow sensor was used: *Si* substrate that is 500 μm thick, 2.2 μm *SiO*₂ layer sandwiched between *Si* and 220 nm thick *Si*₃*N*₄ at the outer (Figure 4.1a).

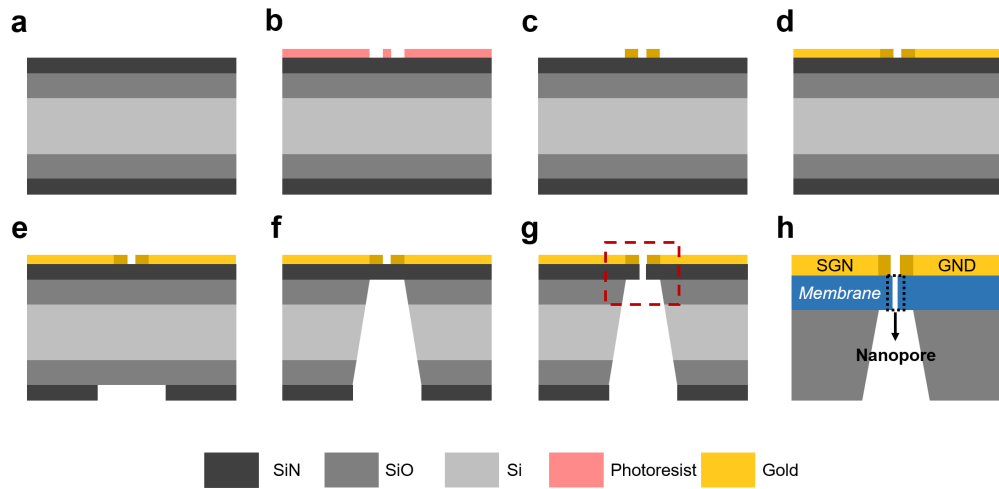


Figure 4.1: Flow schematics for fabrication

In this case, two sensing electrodes were separated by hundreds of nanometer instead of dozens of micrometer, therefore, an additional electron beam lithography (EBL) step was performed to pattern electrodes (Figure 4.1b). Figure 4.2 shows the SEM image of the electrodes separated by 500 nm patterned after EBL, here the membrane & nanopore have not been formed yet.

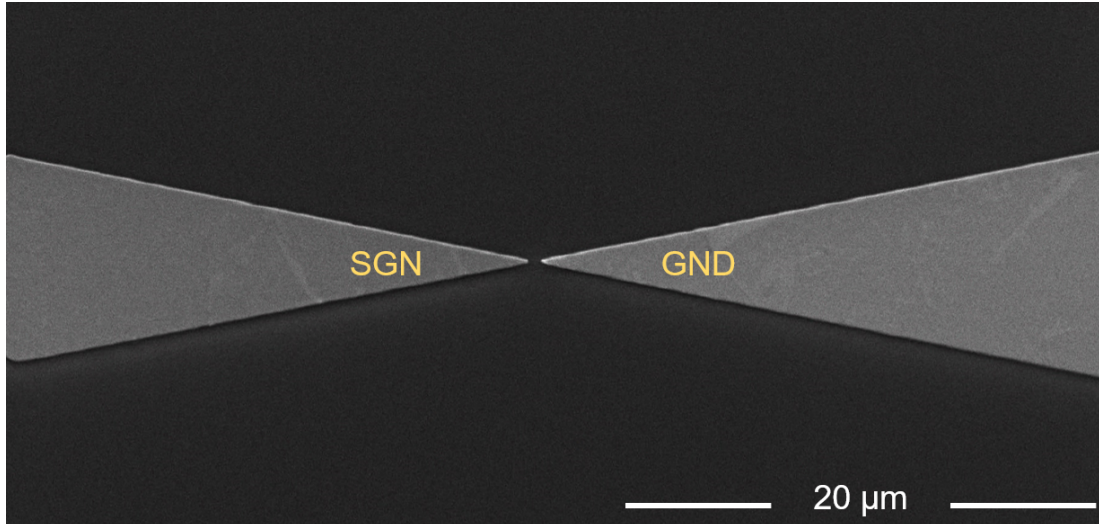


Figure 4.2: Electrodes after EBL process

EBL generally do not have a very large write field area so only a small portion of the electrodes was patterned and coated with 10 nm chromium & 100 nm gold with thermal evaporation (Figure 4.1c). Then, with the designed mask, the rest of the electrodes were patterned and aligned to the prior electrodes with photolithography process (Figure 4.1d). UV exposed chip was coated with 10 nm chromium & 100 nm gold. At the bottom of the wafer, a window was opened with the anisotropic etching of Si_3N_4 (Figure 4.1e). From this window, the membrane was suspended by KOH wet etching of Si & SiO_2 until the top Si_3N_4 layer (Figure 4.1f). The membrane window should be aligned with the electrodes at the top so that the nanopore can be drilled in between the sensing electrodes. In the last step, the chip was placed inside the Focused Ion Beam (FIB) chamber, and by bombarding the electrons, a hole was formed on the membrane in between the sensing electrodes (Figure 4.1g). In the final configuration, electrodes were aligned on the membrane and the nanopore was in between the electrodes having typically 200 - 700 nm diameter depending on the separation between the electrodes after EBL (i.e. accuracy of EBL step).

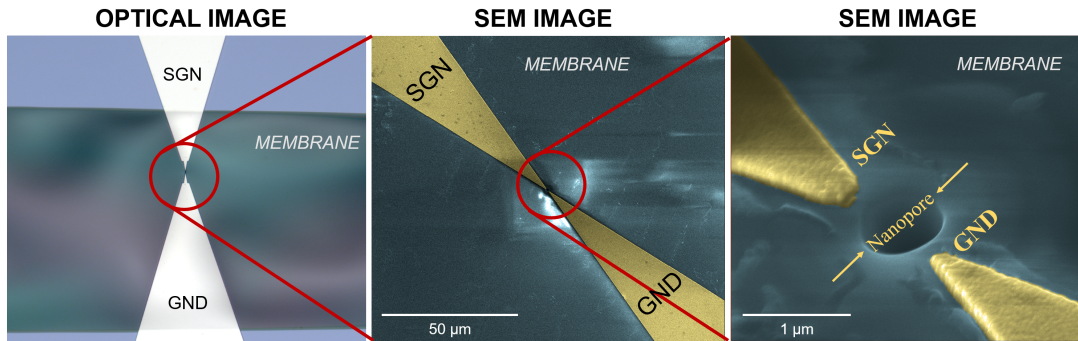


Figure 4.3: Fabricated electrodes

After the cleanroom process, a reservoir that will be referred to as particle reservoir in the upcoming sections was sealed to the bottom of the wafer aligned to the membrane window and finally SMA connection was made.

4.2 Experimental Setup

Contrary to previous chapters, the chip was not placed under the optical microscope, yet, it was still inside the Faraday cage during the experiments. Sensing electrodes and the membrane region of the chip were submerged into an ionic liquid solution, namely Dulbecco's Phosphate Buffered Saline (DPBS), but SMA connection remained outside of the liquid (Figure 4.4a). Realize that in Figure 4.4a, the bottom of the chip is seen, and top of the chip where the electrodes and membranes were patterned were submerged into the liquid.

Then required electronic connections were made together with an electrokinetic setup consisting of a sourcemeter (Keithley 2401) and two copper wires: top and bottom wires. The bottom wire was placed inside the large reservoir where the sensing region and membrane of the chip were also dipped into and the top wire was placed inside the particle reservoir (Figure 4.4b).

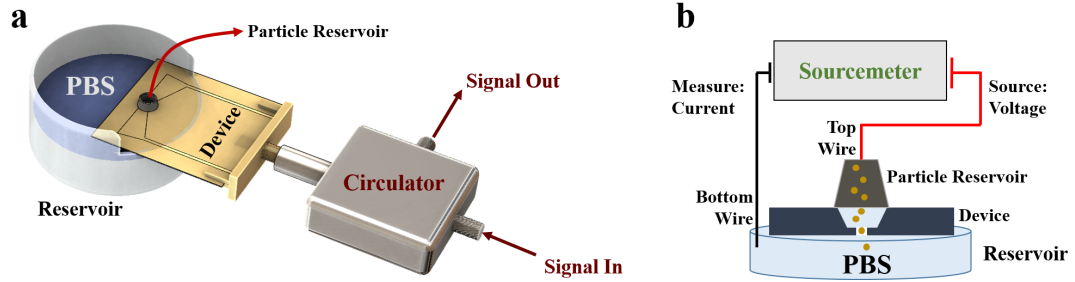


Figure 4.4: Experimental configuration

4.3 Nanopore and I-V Curve Measurements

For electrokinetic motion, several nanopore applications use Ag/AgCl reference electrodes to overcome electrical double layer formation. However, after estimating the resistance of the nanopore and recording the I-V curve, copper wires seemed to give accurate current values.

The resistance of the pore was estimated using Equation 4.1 where ρ is the resistivity of PBS solution, in the datasheet conductivity of PBS ($\sigma = \frac{1}{\rho}$) was reported as 16 mS/cm and it was 15.67 mS/cm when it was measured by the conductivity meter. L is the length of the pore which corresponds to the membrane thickness: 220 nm and A represents the area of the pore, here the pore was assumed to have a square area with a side length of 400 nm.

$$R = \rho \frac{L}{A} \quad (4.1)$$

The resistance of the nanopore, R , turns out to be $\approx 1.0 \text{ M}\Omega$ and uncertainty in the nanopore resistance, which comes from the size variations ($\approx 20 \text{ nm}$) in each SEM measurements, is estimated to be around $\approx 0.1 \text{ M}\Omega$. Then using one of the newly fabricated devices, having the same dimensions in the estimation,

the I-V curve was recorded as depicted in Figure 4.5. Both estimated values from Equation 4.1 and experimental values were plotted on the same graph (Figure 4.5). A linear fit to the experimental data was also illustrated.

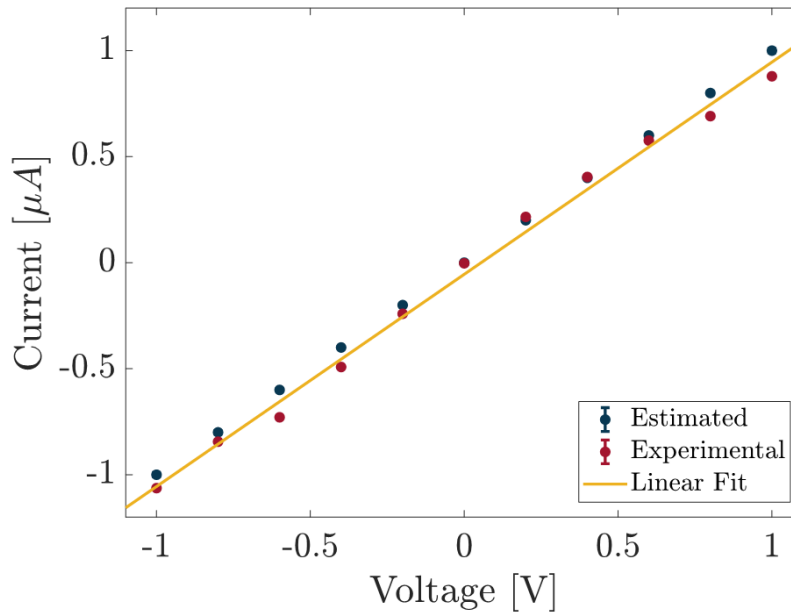


Figure 4.5: I-V curve measurement

When -1 V was applied, the current value on the sourcemeter was $-1.06 \mu\text{A}$, in fact, the resistance of the nanopore, was $\approx 1.0 \text{ M}\Omega$, therefore, the current value should be around $-1.0 \mu\text{A}$ which is the case in the experimental setup. When +1.0 V was applied, the current value was $+0.88 \mu\text{A}$. Therefore, there is a linear relation between the source voltage and the measured current when copper wires were employed.

For the validation and accuracy of the experiment, electrodes were placed to different locations while applying -0.5 V , and measured current values were noted in different trials. If two electrodes were placed inside the large reservoir filled with PBS, the current value was typically around $30 - 50 \mu\text{A}$. If two electrodes were placed into different reservoir and if two reservoirs were interconnected at nanopore, the current value was typically between $10 - 200 \text{ nA}$ depending on the pore size.

If there were no connection between the large reservoir and particle reservoir (e.g. pore was clogged or the device was not submerged deep enough into PBS), the current value fluctuates in the order of dozens of pA. If the membrane was broken, the current value was around $5 - 10 \mu\text{A}$. PLL would not be able to lock to resonance frequency as the sensing electrodes were also on the membrane in the case of the membrane was broken. Additionally, there might be leakage from the sealing of the particle reservoir to the large reservoir which can happen after several experiments. In this case, the measured current value is around $5 - 10 \mu\text{A}$. Therefore, before starting the experiment, the interconnection of the reservoirs and integrity of the membrane should be double-checked.

4.4 Experimental Results

In the first trials with gold nanoparticles, neither PBS nor sourcemeter were integrated into the experimental setup. Instead, DI water and voltage source were used in the system and positive voltage value was applied. After the optimizations, data taken with polystyrene particles, and Felocell Vaccine were recorded with PBS and sourcemeter.

4.4.1 Gold Nanoparticle Experiments

20 nm gold nanoparticles were employed in the earlier experiments and the resonance frequency of the fabricated device was tracked at 7.06 GHz with Allan Deviation of 1×10^{-8} . Then 0.8 V was applied from voltage source.

In the control run, the particle reservoir was filled with DI water and no particle was added. While the resonance frequency was tracked with PLL circuitry, no precipitous jumps were recorded, however, after adding the particles to the reservoir and translocating them electrokinetically, sudden jumps were observed in the frequency track. Figure 4.6 shows an example of the recorded data.

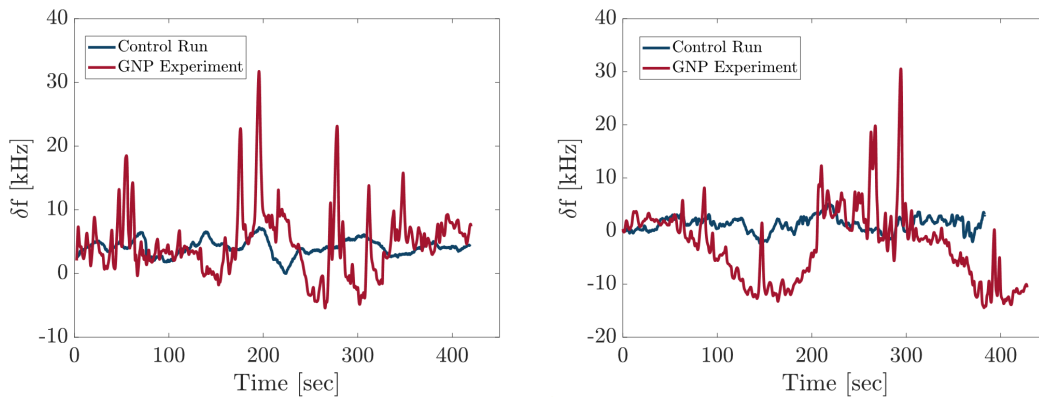


Figure 4.6: Gold nanoparticle experiment

In the particle run, more drift was observed in the frequency which might be a case due to particle passages through the pore.

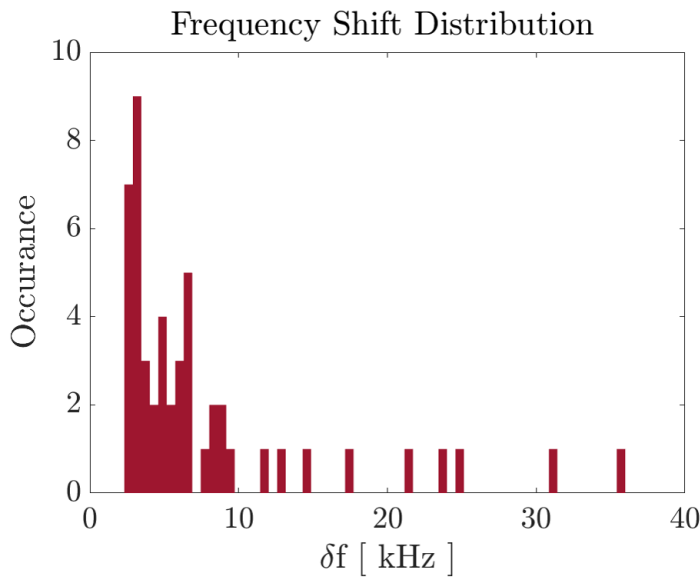


Figure 4.7: Histogram of gold nanoparticles

Data obtained were analyzed and the histogram for the frequency shifts were extracted as in Figure 4.7. The shifts were concentrated around 3 kHz, however, there were larger shifts (e.g. 36 kHz) which were thought to be induced by chains of gold nanoparticles (e.g. chain with 12 gold nanoparticles). In fact, other large

shifts were also multiple of 3 kHz that can represent different chain lengths. After the experiment, the sensing region of the device was checked under SEM, however, there was no gold nanoparticle aggregated around the sensing electrodes.

4.4.2 Design Optimization & Faster Data Recording

In the first design (Figure 4.8a), the resonance amplitude of the S21 parameter was around -5 dB and some devices did not have any resonant point. To have an explicit and sensitive resonance, the electric field was intensified by patterning sharper electrodes around the nanopore. For that purpose, two electrodes were patterned such that they started to converge each other at an earlier point (Figure 4.8b) as a result -15 to -20 dB resonance was achieved.

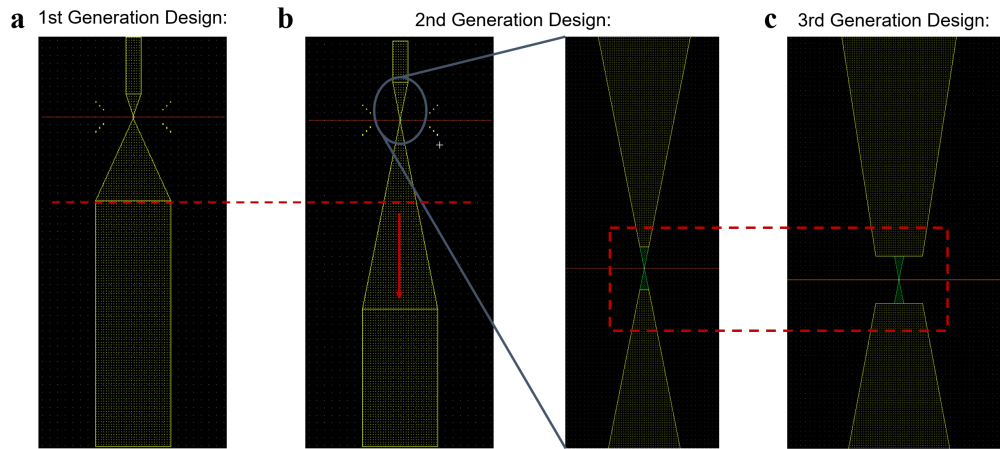


Figure 4.8: Design improvement

As a slight improvement, a protrusion was introduced to concentrate the electric field at the sharp tip (Figure 4.8c). This improved resonance amplitude to -20 to -25 dB in S21 parameter (Figure 4.9).

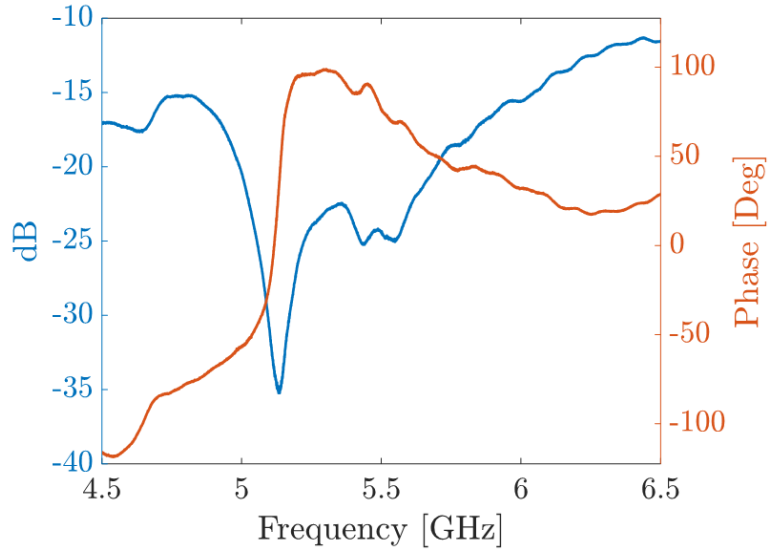


Figure 4.9: S21 VNA response after optimizations

After optimizing the resonance of the device, the data transfer rate was also enhanced using a CompactRIO(cRIO) with an analog input module (NI 9775). In this way, the phase response of the resonator can be recorded every $20 \mu\text{s}$ while the lock-in amplifier time constant was set to $50 \mu\text{s}$. The AUX output of the lock-in amplifier was connected to the analog input module on cRIO to read phase value.

At high sampling rates and small lock in time constant values, at the end of each LabVIEW loop ($\approx 50 \text{ ms}$), there was an interference between LabVIEW & cRio and spikes were observed in the phase data. In the short term, this problem was forestalled by locking the resonator to the resonance frequency then stopping LabVIEW loop. Since the proposed resonator has low-quality factor (≈ 100), compared to a NEMS resonator, the resonator still dwells around the resonance frequency and responsive to the external effects.

4.4.3 Polystyrene Particle Experiments

After device & measurement improvements, early experiments were performed by using standard-sized polystyrene nanoparticle (50 and 100 nm). Samples prepared for the experiments were diluted with PBS and particle solution formed 1 - 2% of the overall solution. The original particle solution consists of 99% of DI water and 1% polystyrene solid content. The sample was mixed with pipetting to separate clustered particles. Typically, 25 – 50 μL was added to the particle reservoir.

4.4.3.1 100 nm Polystyrene Nanoparticle Experiment

The resonance frequency of the device was tracked at 6.61 GHz with a lock-in time constant of 50 μs and the sampling rate of cRIO was 50 kSa/s. The solution used in the experiment had a concentration of 1.5% polystyrene particle. The measured current value in the sourcemeter was in between 12 – 14 nA.

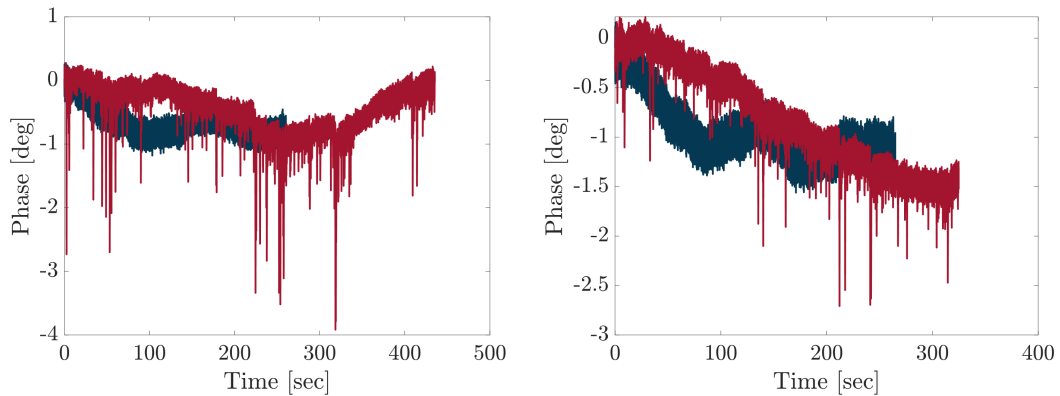


Figure 4.10: 100 nm polystyrene particle

To check the control of the electrokinetic motion, the voltage supplied was decreased to -0.3 V (Figure 4.11a). A dramatic decrease in the phase shifts was observed, then voltage supplied was increased to -0.5 V and more phase modulations were observed (Figure 4.11b). Lastly, the applied voltage was set to -1 V, and compared to Figure 4.11b, more phase shifts were recorded (Figure

4.11c).

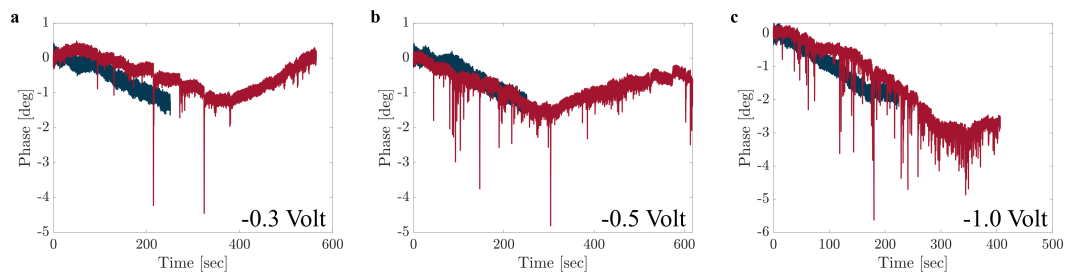


Figure 4.11: Control over electrokinetic motion

Therefore, there was control over the particle transition through the nanopore. After data were recorded and analyzed, the histogram phase shifts were concentrated around 1.1 degrees which was expected as polystyrene nanoparticles were similarly sized (Figure 4.12).

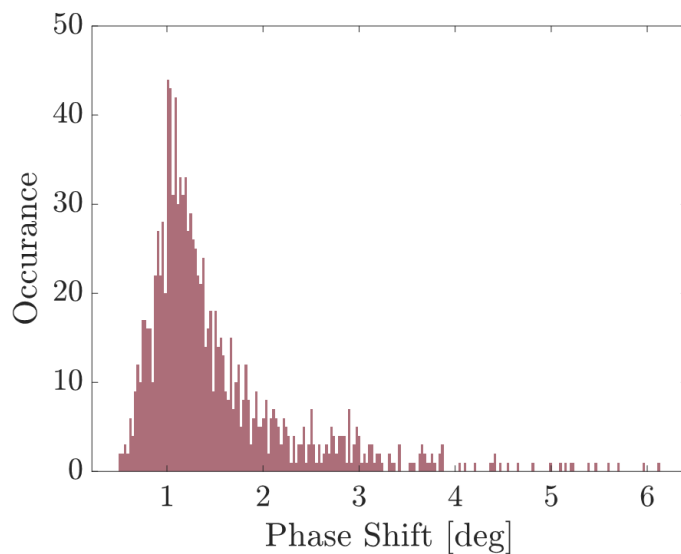


Figure 4.12: Histogram for 100 nm polystyrene particle

4.4.3.2 50 nm Polystyrene Nanoparticle Experiment

The resonance frequency of the resonator was tracked at 7.19 GHz with lock-in time constant of 50 μs and sampling rate of 50 kSa/s. The solution used in the experiment had a concentration of 1% polystyrene particle. The measured current value in the sourcemeter was in between 170 – 185 nA.

In the control run, there was not any sudden jump in the phase, yet, when particles were added due to the particle transition phase of the resonator was modulated (Figure 4.13).

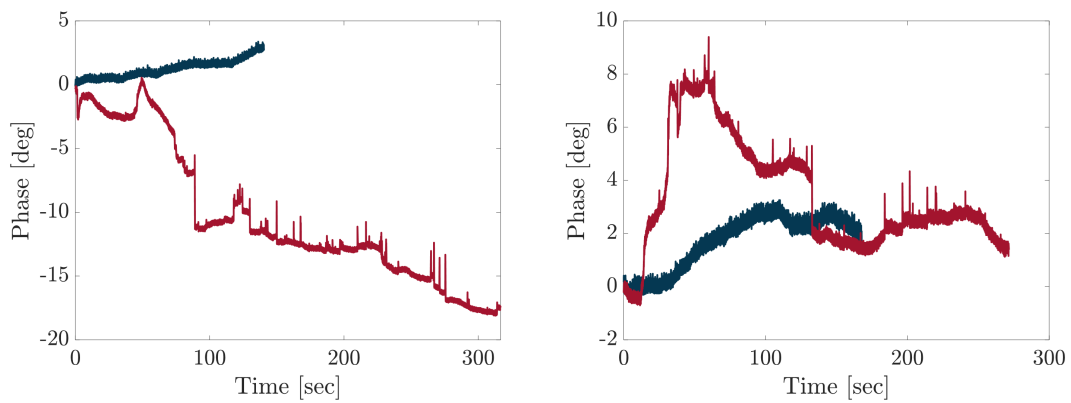


Figure 4.13: 50 nm polystyrene particle

Compared to phase shifts in Figure 4.10 and Figure 4.11, there were fewer jumps this might happen as the new solution was less concentrated (1%) compared to the previous solution(1.5%).

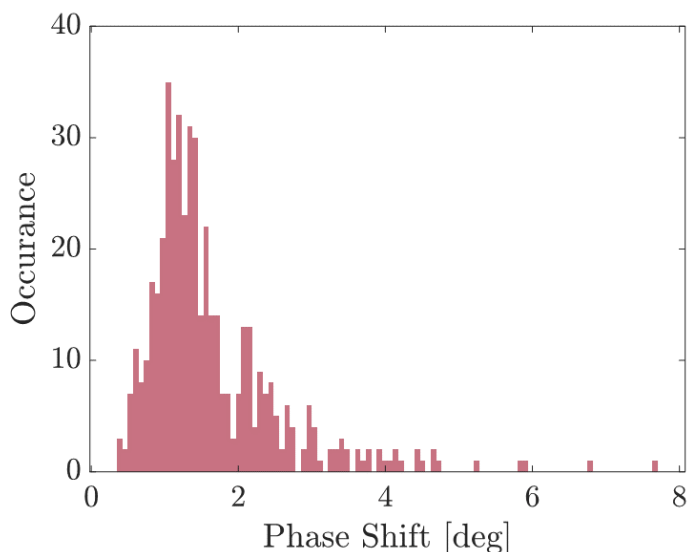


Figure 4.14: Histogram for 50 nm polystyrene particle

After data were recorded and analyzed, in the histogram (Figure 4.14) phase shifts were concentrated around 1.1 degrees which was expected as polystyrene nanoparticles almost have a similar size. Using the same analysis method, control runs were also analyzed and most of the shifts were around 0.3 degrees which was the noise level during the experiment.

4.4.4 Felocell Vaccine Experiments

To assess the performance of the microwave resonator with biological samples, Felocell CVR which is a generic vaccine for cats was used. Felocell CVR consists of Feline Rhinotracheitis Virus, Calicivirus, and Panleukopenia Virus which are not hazardous to humans. The vaccine was in lyophilized form, so it was reconstituted with PBS and filtered with a 220 nm pore sized filter. The reported diameter of the viruses are as follows: Feline Rhinotracheitis: 150–200 nm, Calicivirus: 35–39 nm, Panleukopenia: 18–22 nm. After the mixture was pipetted to forestall clustering, 50 μL of viruses in PBS was added to the particle reservoir.

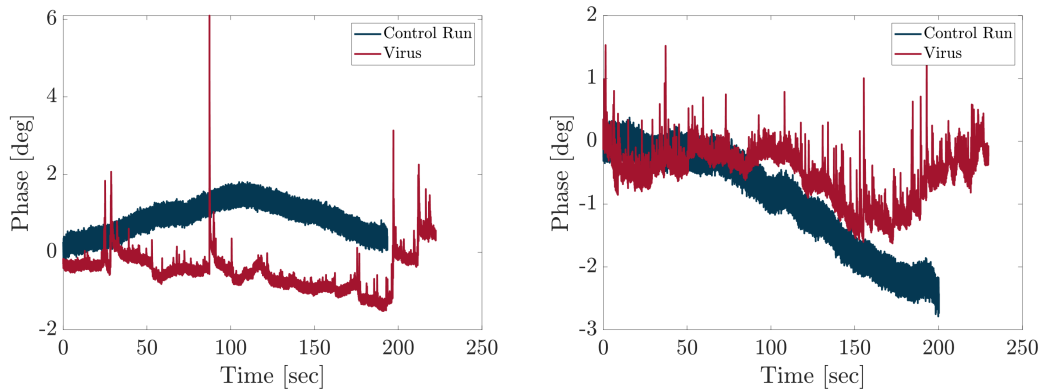


Figure 4.15: Felocell CVR experiment

The resonance frequency was tracked at 5.18 GHz and a similar experimental procedure was followed yielding similar results. There were no precipitous jumps in the control run where there were no viruses, however, after viruses were added to the reservoir, the phase of the resonator was modulated.

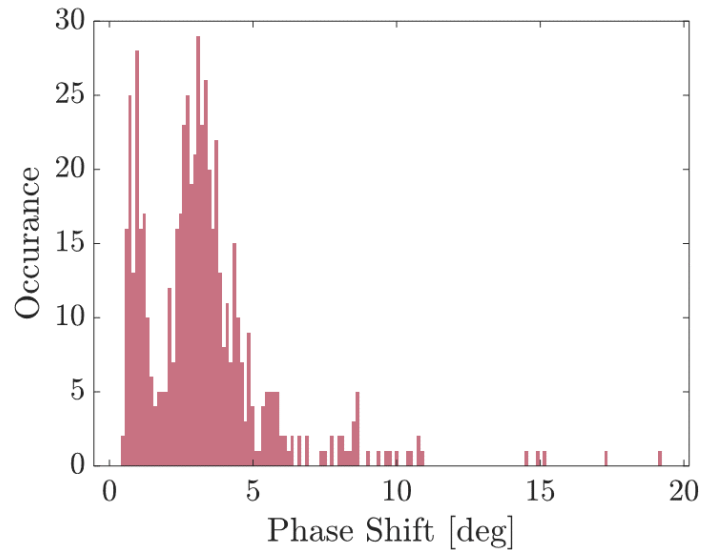


Figure 4.16: Histogram of the phase shifts in Felocell CVR experiment

As explained earlier, there are 3 different viruses in the vaccine, and 3 distinct peaks around 0.7, 1 and 3.1 degrees may correspond to the response of each type

of virus (Figure 4.16). The size of the smallest one (Panleukopenia) was 18–22 nm and 0.7 degree shift might be induced by that one. Mid-one was 35–39 nm and 1 degree shift might be induced by that one which is close to the previous one in size but slightly larger. The largest one (Rhinotracheitis) has the largest dispersion 150–200 nm and wide distribution around 3 degrees may be interpreted as the response induced by the Rhinotracheitis virus.

Chapter 5

Conclusion & Future Perspective

In this chapter, a summary of the proposed applications will be given and their future perspective will be envisaged.

5.1 Single Cell Detection

The first application was to detect single cells and relate their electrical volume to the geometrical volume. For the electrical volume, cells were made a pass through the sensing electrodes and the frequency changes of the resonator were recorded. Dispersions due to sensor geometry were elucidated by changing the dimensions of the device and using standard-sized particles. The frequency response of a single cell was also recorded over a while and its optical images were analyzed through a custom-built image processing algorithm. Cells were also treated with DMSO to observe the change in their morphology and as DMSO expedites cytolysis, the expected decrease in the resonance shifts was observed over a time period.

The priority should be eliminating the positional dependency and designing a more sensitive microwave resonator. The aforementioned suspended microchannel resonators are one order more sensitive than the proposed microwave resonator. However, thanks to the ease of fabrication of the microwave resonators,

improvements in the device volume and noise level can be made expeditiously.

In the next generation, a split ring resonator (SRR) design was proposed. This time, microwave signal does not propagate through the electrodes, rather, it is coupled to a split ring resonator that has the closest gap of 20 μm . With this device, the first experiments were done using standard-sized particles again and the resonance frequency of the design was around 5 GHz. Considering the same channel height for two different designs (Bow tie CPW and SRR), the amount of the shift increased to ≈ 160 kHz from ≈ 30 kHz. On average, the sensitivity of the resonator was improved 4 times. (From $1 \times 10^{-3} \text{kHz}/\mu\text{m}^3$ to $4 \times 10^{-3} \text{kHz}/\mu\text{m}^3$) However, the noise level in the new design was around 1 - 1.5 kHz, therefore, there was not a significant improvement in the signal to noise ratio (SNR). Yet, more investigation is still needed to reduce noise levels.

By integrating a more complex microchannel geometry, the response of a single cell to a certain drug can be examined. This can be crucial to determine the most effective drug for a chemotherapy treatment at a single-cell level. To observe the response over a long period, an incubation system is needed to maintain cell vitality. Commercial microscopy integrated incubator disturbed the microwave signals when the chip was placed on it, so in the next step more effective incubation system should be built. Then, cell response to a specific drug can be observed.

At this point, the cell line to be used is important. In this thesis, MDA-MB-231-LUC2-GFP breast cancer cell line was cultured which was previously and stably labeled with luciferase and green fluorescent protein (GFP). This cell line grows as a monolayer enabling to culture them in cell culture dishes where the surface is pre-treated to allow the adhesion of anchor-dependent cells. Although this system has been used for several years and is still a dominant cell culture method, it is two-dimensional (2D) which has a low capacity to imitate *in vivo* conditions. Recently, three-dimensional (3D) cell culture methods are being used to mimic the proper tissue physiology and multicellular organisms [102]. In other words, cells grown in 3D cultures show more adaptive characteristics to their environment than the ones grown in 2D cultures [103]. To create 3D cultures,

dishes can be coated with a matrix gel such as fibronectin (an extracellular matrix protein) which will increase the rate of cell adhesion [102, 104]. Similarly, microchannel can be coated with a matrix gel and cells can be cultured within the channel and simultaneously their microwave response can be observed.

5.2 Nanomechanical Flow Rate Sensor

In the second application, wrinkles on a nanomembrane were converted to a flow rate sensing mechanism. The instability induced by the fluid flow modulates the resonance of the sensor within a time proportional to the flow rate. Then by fabricating devices with different membrane and channel dimensions, various flow rate intervals were spanned until the upper limit of the reference flow rate sensor. It was observed that for each flow rate value there is a specific pulsation frequency in the resonance. Then a secondary sensing mechanism was proposed to determine the flow rate from reset. The amount of frequency shift until the target flow rate value is distinct to the effective flow rate inside the channel. In the next step, similar experiments were conducted by pressurizing air instead of DI water using the secondary sensing mechanism. While the reference sensor cannot measure the airflow rate, the flow rate was estimated through a calibration procedure using DI water. It was recorded that for each airflow rate, the amount of shift is again specific. The membrane could also endure up to 4 bars during the experiment.

The proposed technology can be converted to an on-chip flow rate sensor platform just by design optimizations and packaging of the measurement circuitry. On-chip flow rate sensors are extremely useful for the precise delivery of drug/nutrients in lab/organ-on-a-chip applications as the actual flow rate within the microchannel might be different from what is read by a commercial sensor.

The sensor can be also used for observing fluid-fluid interaction such as droplet formation. The size of the droplet depends on the effective flow rate and for precise droplet formation, the proposed sensor can be used to determine the

effective flow rate and can also measure the size of the droplet as explained earlier with cells. The pulsation behavior of the membrane can be also utilized as an on-chip pump in more advanced applications.

5.3 Nanopore Sensing of Viruses

In the last application, a nanopore integrated microwave resonator was employed to detect nanoscale analytes. The same bow tie electrodes this time narrowed down to hundreds of nanometer and a pore was drilled in between the electrodes. Using electrokinetic motion, analytes were made a pass through a pore which modulates the phase of the chip. Initial experiments were done with gold nanoparticles and after the design and experimental setup improvements, experiments were conducted with polystyrene particles and viruses.

The sensitivity of the resonator can be enhanced by building the electrodes encapsulating the nanopore with a semi-circle shape. For this, first, fine control in EBL and FIB steps is primarily required. Also, a microwave resonator with a split ring design (that is explained in Chapter 5.1) can be fabricated to enhance the sensitivity.

Lastly, building a nanochannel around the sensing electrodes and translocating the analytes as explained in the cell part can alleviate the ambiguity of nanopore and fluidic damping.

Bibliography

- [1] M. Mir, Z. Wang, Z. Shen, M. Bednarz, R. Bashir, I. Golding, S. G. Prasanth, and G. Popescu, “Optical measurement of cycle-dependent cell growth,” *Proceedings of the National Academy of Sciences*, vol. 108, no. 32, pp. 13124–13129, 2011.
- [2] P. Rosendahl, K. Plak, A. Jacobi, M. Kraeter, N. Toepfner, O. Otto, C. Herold, M. Winzi, M. Herbig, and Y. e. a. Ge, “Real-time fluorescence and deformability cytometry,” *Nature Methods*, vol. 15, no. 5, pp. 355–358, 2018.
- [3] G. Popescu, Y. Park, N. Lue, C. Best-Popescu, L. Deflores, R. R. Dasari, M. S. Feld, and K. Badizadegan, “Optical imaging of cell mass and growth dynamics,” *American Journal of Physiology-Cell Physiology*, vol. 295, no. 2, pp. C538–C544, 2008.
- [4] Y. Park, C. Depeursinge, and G. Popescu, “Quantitative phase imaging in biomedicine,” *Nature Photonics*, vol. 12, no. 10, pp. 578–589, 2018.
- [5] T. P. Burg, M. Godin, S. M. Knudsen, W. Shen, G. Carlson, J. S. Foster, K. Babcock, and S. R. Manalis, “Weighing of biomolecules, single cells and single nanoparticles in fluid,” *Nature*, vol. 446, no. 7139, pp. 1066–1069, 2007.
- [6] M. Godin, F. F. Delgado, S. Son, W. H. Grover, A. K. Bryan, A. Tzur, P. Jorgensen, K. Payer, A. D. Grossman, and M. W. e. a. Kirschner, “Using buoyant mass to measure the growth of single cells,” *Nature Methods*, vol. 7, no. 5, pp. 387–390, 2010.

- [7] W. H. Grover, A. K. Bryan, M. Diez-Silva, S. Suresh, J. M. Higgins, and S. R. Manalis, “Measuring single-cell density,” *Proceedings of the National Academy of Sciences*, vol. 108, no. 27, pp. 10992–10996, 2011.
- [8] K. Park, A. Mehrnezhad, E. A. Corbin, and R. Bashir, “Optomechanical measurement of the stiffness of single adherent cells,” *Lab on a Chip*, vol. 15, no. 17, pp. 3460–3464, 2015.
- [9] N. Cermak, S. Olcum, F. F. Delgado, S. C. Wasserman, K. R. Payer, M. A. Murakami, S. M. Knudsen, R. J. Kimmerling, M. M. Stevens, and Y. e. a. Kikuchi, “High-throughput measurement of single-cell growth rates using serial microfluidic mass sensor arrays,” *Nature Biotechnology*, vol. 34, no. 10, 2016.
- [10] A. Martin-Perez, D. Ramos, E. Gil-Santos, S. Garcia-Lopez, M. L. Yubero, P. M. Kosaka, A. San Paulo, J. Tamayo, and M. Calleja, “Mechano-optical analysis of single cells with transparent microcapillary resonators,” *ACS Sensors*, vol. 4, no. 12, pp. 3325–3332, 2019.
- [11] D. Martinez-Martin, G. Flaschner, B. Gaub, S. Martin, R. Newton, C. Beerli, J. Mercer, C. Gerber, and D. J. Muller, “Inertial picobalance reveals fast mass fluctuations in mammalian cells,” *Nature*, vol. 550, no. 7677, pp. 500–505, 2017.
- [12] A. E. Cetin, M. M. Stevens, N. L. Calistri, M. Fulciniti, S. Olcum, R. J. Kimmerling, N. C. Munshi, and S. R. Manalis, “Determining therapeutic susceptibility in multiple myeloma by single-cell mass accumulation,” *Nature Communications*, vol. 8, no. 1, 2017.
- [13] S. Olcum, N. Cermak, S. C. Wasserman, K. S. Christine, H. Atsumi, K. R. Payer, W. Shen, J. Lee, A. M. Belcher, and S. N. e. a. Bhatia, “Weighing nanoparticles in solution at the attogram scale,” *Proceedings of the National Academy of Sciences*, vol. 111, no. 4, pp. 1310–1315, 2014.

- [14] K. Park, L. J. Millet, N. Kim, H. Li, X. Jin, G. Popescu, N. R. Aluru, K. J. Hsia, and R. Bashir, “Measurement of adherent cell mass and growth,” *Proceedings of the National Academy of Sciences*, vol. 107, no. 48, pp. 20691–20696, 2010.
- [15] N. Maloney, G. Lukacs, J. Jensen, and M. Hegner, “Nanomechanical sensors for single microbial cell growth monitoring,” *Nanoscale*, vol. 6, no. 14, pp. 8242–8249, 2014.
- [16] O. Malvar, J. J. Ruz, P. M. Kosaka, C. M. Dominguez, E. Gil-Santos, M. Calleja, and J. Tamayo, “Mass and stiffness spectrometry of nanoparticles and whole intact bacteria by multimode nanomechanical resonators,” *Nature Communications*, vol. 7, no. 1, 2016.
- [17] T. P. Burg and S. R. Manalis, “Suspended microchannel resonators for biomolecular detection,” *Applied Physics Letters*, vol. 83, no. 13, pp. 2698–2700, 2003.
- [18] M. Godin, A. K. Bryan, T. P. Burg, K. Babcock, and S. R. Manalis, “Measuring the mass, density, and size of particles and cells using a suspended microchannel resonator,” *Applied Physics Letters*, vol. 91, no. 12, p. 123121, 2007.
- [19] J. Lee, W. Shen, K. Payer, T. P. Burg, and S. R. Manalis, “Toward attogram mass measurements in solution with suspended nanochannel resonators,” *Nano Letters*, vol. 10, no. 7, pp. 2537–2542, 2010.
- [20] S. Olcum, N. Cermak, S. C. Wasserman, and S. R. Manalis, “High-speed multiple-mode mass-sensing resolves dynamic nanoscale mass distributions,” *Nature Communications*, vol. 6, no. 1.
- [21] M. Gagino, G. Katsikis, S. Olcum, L. Viro, M. Cochet, A. Thuaire, S. R. Manalis, and V. Agache, “Suspended nanochannel resonator arrays with piezoresistive sensors for high-throughput weighing of nanoparticles in solution,” *ACS Sensors*, vol. 5, no. 4, pp. 1230–1238, 2020.

- [22] H. Etayash, M. F. Khan, K. Kaur, and T. Thundat, “Microfluidic cantilever detects bacteria and measures their susceptibility to antibiotics in small confined volumes,” *Nature Communications*, vol. 7, no. 1, 2016.
- [23] J. Kim, J. Song, K. Kim, S. Kim, J. Song, N. Kim, M. F. Khan, L. Zhang, J. E. Sader, and K. e. a. Park, “Hollow microtube resonators via silicon self-assembly toward subattogram mass sensing applications,” *Nano Letters*, vol. 16, no. 3, pp. 1537–1545, 2016.
- [24] D. Lee, J. Kim, N.-J. Cho, T. Kang, S. Kauh, and J. Lee, “Pulled microcapillary tube resonators with electrical readout for mass sensing applications,” *Scientific Reports*, vol. 6, no. 1, 2016.
- [25] M. K. Ghatkesar, H. H. P. Garza, and U. Staufer, “Hollow afm cantilever pipette,” *Microelectronic Engineering*, vol. 124, pp. 22–25, 2014.
- [26] A. De Pastina, D. Maillard, and L. Villanueva, “Fabrication of suspended microchannel resonators with integrated piezoelectric transduction,” *Microelectronic Engineering*, vol. 192, pp. 83–87, 2018.
- [27] M. Faheem Khan, S. Kim, D. Lee, S. Schmid, A. Boisen, and T. Thundat, “Nanomechanical identification of liquid reagents in a microfluidic channel,” *Lab Chip*, vol. 14, no. 7, pp. 1302–1307, 2014.
- [28] G. A. Ferrier, S. F. Romanuik, D. J. Thomson, G. E. Bridges, and M. R. Freeman, “A microwave interferometric system for simultaneous actuation and detection of single biological cells,” *Lab on a Chip*, vol. 9, no. 23, p. 3406, 2009.
- [29] M. Nikolic-Jaric, S. F. Romanuik, G. A. Ferrier, G. E. Bridges, M. Butler, K. Sunley, D. J. Thomson, and M. R. Freeman, “Microwave frequency sensor for detection of biological cells in microfluidic channels,” *Biomicrofluidics*, vol. 3, no. 3, p. 034103, 2009.
- [30] Y. Yang, H. Zhang, J. Zhu, G. Wang, T.-R. Tzeng, X. Xuan, K. Huang, and P. Wang, “Distinguishing the viability of a single yeast cell with an ultra-sensitive radio frequency sensor,” *Lab on a Chip*, vol. 10, no. 5, p. 553, 2010.

- [31] C. Dalmay, M. Cheray, A. Pothier, F. Lalloue, M. Jauberteau, and P. Blondy, “Ultra sensitive biosensor based on impedance spectroscopy at microwave frequencies for cell scale analysis,” *Sensors and Actuators A: Physical*, vol. 162, no. 2, pp. 189–197, 2010.
- [32] J.-C. Chien, A. Ameri, E.-C. Yeh, A. N. Killilea, M. Anwar, and A. M. Niknejad, “A high-throughput flow cytometry-on-a-cmos platform for single-cell dielectric spectroscopy at microwave frequencies,” *Lab on a Chip*, vol. 18, no. 14, pp. 2065–2076, 2018.
- [33] C. Watts, S. M. Hanham, J. P. K. Armstrong, M. M. Ahmad, M. M. Stevens, and N. Klein, “Microwave dielectric sensing of free-flowing, single, living cells in aqueous suspension,” *IEEE Journal of Electromagnetics, RF and Microwaves in Medicine and Biology*, vol. 4, no. 2, pp. 97–108, 2020.
- [34] K. L. Ekinici, V. Yakhot, S. Rajauria, C. Colosqui, and D. M. Karabacak, “High-frequency nanofluidics: a universal formulation of the fluid dynamics of mems and nems,” *Lab on a Chip*, vol. 10, no. 22, p. 3013, 2010.
- [35] V. Kara, Y.-I. Sohn, H. Atikian, V. Yakhot, M. Loncar, and K. L. Ekinici, “Nanofluidics of single-crystal diamond nanomechanical resonators,” *Nano Letters*, vol. 15, no. 12, pp. 8070–8076, 2015.
- [36] J. E. Sader, “Frequency response of cantilever beams immersed in viscous fluids with applications to the atomic force microscope,” *Journal of Applied Physics*, vol. 84, no. 1, pp. 64–76, 1998.
- [37] J. E. Sader, J. Lee, and S. R. Manalis, “Energy dissipation in microfluidic beam resonators: Dependence on mode number,” *Journal of Applied Physics*, vol. 108, no. 11, p. 114507, 2010.
- [38] J. H. Kang, T. P. Miettinen, L. Chen, S. Olcum, G. Katsikis, P. S. Doyle, and S. R. Manalis, “Noninvasive monitoring of single-cell mechanics by acoustic scattering,” *Nature Methods*, vol. 16, no. 3, pp. 263–269, 2019.

- [39] T. P. Burg, J. E. Sader, and S. R. Manalis, “Nonmonotonic energy dissipation in microfluidic resonators,” *Physical Review Letters*, vol. 102, no. 22, 2009.
- [40] M. Argentina and L. Mahadevan, “Fluid-flow-induced flutter of a flag,” *Proceedings of the National Academy of Sciences*, vol. 102, no. 6, pp. 1829–1834, 2005.
- [41] Y. WATANABE, S. SUZUKI, M. SUGIHARA, and Y. SUEOKA, “An experimental study of paper flutter,” *Journal of Fluids and Structures*, vol. 16, no. 4, pp. 529–542, 2002.
- [42] C. Eloy, C. Souilliez, and Schou, “Flutter of a rectangular plate,” *Journal of Fluids and Structures*, vol. 23, no. 6.
- [43] M. M. Stevens, C. L. Maire, N. Chou, M. A. Murakami, D. S. Knoff, Y. Kikuchi, R. J. Kimmerling, H. Liu, S. Haidar, and N. L. e. a. Calistri, “Drug sensitivity of single cancer cells is predicted by changes in mass accumulation rate,” *Nature Biotechnology*, vol. 34, no. 11, pp. 1161–1167, 2016.
- [44] T. Ward, M. Faivre, M. Abkarian, and H. A. Stone, “Microfluidic flow focusing: Drop size and scaling in pressure versus flow-rate-driven pumping,” *ELECTROPHORESIS*, vol. 26, no. 19, pp. 3716–3724, 2005.
- [45] P. Garstecki, M. J. Fuerstman, H. A. Stone, and G. M. Whitesides, “Formation of droplets and bubbles in a microfluidic t-junction scaling and mechanism of break-up,” *Lab on a Chip*, vol. 6, no. 3, p. 437, 2006.
- [46] T. Glawdel, C. Elbuken, and C. L. Ren, “Droplet formation in microfluidic t-junction generators operating in the transitional regime. i. experimental observations,” *Physical Review E*, vol. 85, no. 1, 2012.
- [47] J. T. W. Kuo, L. Yu, and E. Meng, “Micromachined thermal flow sensors - a review,” *Micromachines*, vol. 3, no. 3, pp. 550–573, 2012.

- [48] A. Baldwin, L. Yu, and E. Meng, “An electrochemical impedance-based thermal flow sensor for physiological fluids,” *Journal of Microelectromechanical Systems*, vol. 25, no. 6, pp. 1015–1024, 2016.
- [49] J. Kim, H. Cho, S.-I. Han, A. Han, and K.-H. Han, “A disposable microfluidic flow sensor with a reusable sensing substrate,” *Sensors and Actuators B: Chemical*, vol. 288, pp. 147–154, 2019.
- [50] W.-C. Lin and M. A. Burns, “Low-power micro-fabricated liquid flow-rate sensor,” *Analytical Methods*, vol. 7, no. 9, pp. 3981–3987, 2015.
- [51] J. P. Wissman, K. Sampath, S. E. Freeman, and C. A. Rohde, “Capacitive bio-inspired flow sensing cupula,” *Sensors*, vol. 19, no. 11, p. 2639, 2019.
- [52] M. Tang, F. Liu, J. Lei, Z. Ai, S.-L. Hong, N. Zhang, and K. Liu, “Simple and convenient microfluidic flow rate measurement based on microbubble image velocimetry,” *Microfluidics and Nanofluidics*, vol. 23, no. 11, 2019.
- [53] Z. Chen, Z. Guo, X. Mu, Q. Li, X. Wu, and H. Y. Fu, “Packaged microbubble resonator optofluidic flow rate sensor based on bernoulli effect,” *Optics Express*, vol. 27, no. 25, p. 36932, 2019.
- [54] R. Lindken, M. Rossi, S. Grosse, and J. Westerweel, “Micro-particle image velocimetry (upiv): Recent developments, applications, and guidelines,” *Lab on a Chip*, vol. 9, no. 17, p. 2551, 2009.
- [55] P. Salipante, S. D. Hudson, J. W. Schmidt, and J. D. Wright, “Microparticle tracking velocimetry as a tool for microfluidic flow measurements,” *Experiments in Fluids*, vol. 58, no. 7, 2017.
- [56] L. Stern, A. Bakal, M. Tzur, M. Veinguer, N. Mazurski, N. Cohen, and U. Levy, “Doppler-based flow rate sensing in microfluidic channels,” *Sensors*, vol. 14, no. 9, pp. 16799–16807, 2014.
- [57] L. Campagnolo, M. Nikolic, J. Perchoux, Y. L. Lim, K. Bertling, K. Loubiere, L. Prat, A. D. Rakic, and T. Bosch, “Flow profile measurement in microchannel using the optical feedback interferometry sensing technique,” *Microfluidics and Nanofluidics*, vol. 14, no. 1-2, pp. 113–119, 2012.

- [58] M. Sadegh Cheri, H. Latifi, J. Sadeghi, M. Salehi Moghaddam, H. Shahraki, and H. Hajghassem, “Real-time measurement of flow rate in microfluidic devices using a cantilever-based optofluidic sensor,” *The Analyst*, vol. 139, no. 2, pp. 431–438, 2014.
- [59] N. Noeth, S. Keller, and A. Boisen, “Integrated cantilever-based flow sensors with tunable sensitivity for in-line monitoring of flow fluctuations in microfluidic systems,” *Sensors*, vol. 14, no. 1, pp. 229–244, 2013.
- [60] M. Weglarski, P. Jankowski-Mihulowicz, G. Pitera, D. Jurkow, and M. Dorczynski, “Ltcc flow sensor with rfid interface,” *Sensors*, vol. 20, no. 1, p. 268, 2020.
- [61] M. H. Zarifi, H. Sadabadi, S. H. Hejazi, M. Daneshmand, and A. Sanati-Nezhad, “Noncontact and nonintrusive microwave-microfluidic flow sensor for energy and biomedical engineering,” *Scientific Reports*, vol. 8, no. 1, 2018.
- [62] W. Shi, A. K. Friedman, and L. A. Baker, “Nanopore sensing,” *Analytical Chemistry*, vol. 89, no. 1, pp. 157–188, 2016.
- [63] M. Tokeshi, *Applications of Microfluidic Systems in Biology and Medicine*, vol. 7. Springer, 2019.
- [64] J. Clarke, H.-C. Wu, L. Jayasinghe, A. Patel, S. Reid, and H. Bayley, “Continuous base identification for single-molecule nanopore dna sequencing,” *Nature Nanotechnology*, vol. 4, no. 4, pp. 265–270, 2009.
- [65] I. Derrington, T. Butler, M. Pavlenok, M. Collins, M. Niederweis, and J. Gundlach, “Nanopore sequencing with mspa,” *Biophysical Journal*, vol. 96, no. 3, p. 316a, 2009.
- [66] E. A. Manrao, I. M. Derrington, A. H. Laszlo, K. W. Langford, M. K. Hopper, N. Gillgren, M. Pavlenok, M. Niederweis, and J. H. Gundlach, “Reading dna at single-nucleotide resolution with a mutant mspa nanopore and phi29 dna polymerase,” *Nature Biotechnology*, vol. 30, no. 4, pp. 349–353, 2012.

- [67] B. M. Venkatesan and R. Bashir, “Nanopore sensors for nucleic acid analysis,” *Nature Nanotechnology*, vol. 6, no. 10, pp. 615–624, 2011.
- [68] D. Fologea, M. Gershow, B. Ledden, D. S. McNabb, J. A. Golovchenko, and J. Li, “Detecting single stranded dna with a solid state nanopore,” *Nano Letters*, vol. 5, no. 10, pp. 1905–1909, 2005.
- [69] D. Fologea, J. Uplinger, B. Thomas, D. S. McNabb, and J. Li, “Slowing dna translocation in a solid-state nanopore,” *Nano Letters*, vol. 5, no. 9, pp. 1734–1737, 2005.
- [70] M. Wanunu, “Nanopores: A journey towards dna sequencing,” *Physics of Life Reviews*, vol. 9, no. 2, pp. 125–158, 2012.
- [71] D. e. a. Quick, Loman, “Real-time, portable genome sequencing for ebola surveillance,” *Nature*, vol. 530, pp. 228–232, 2016.
- [72] Z. Siwy, L. Trofin, P. Kohli, L. A. Baker, C. Trautmann, and C. R. Martin, “Protein biosensors based on biofunctionalized conical gold nanotubes,” *Journal of the American Chemical Society*, vol. 127, no. 14, pp. 5000–5001, 2005.
- [73] E. C. Yusko, J. M. Johnson, S. Majd, P. Prangkio, R. C. Rollings, J. Li, J. Yang, and M. Mayer, “Controlling protein translocation through nanopores with bio-inspired fluid walls,” *Nature Nanotechnology*, vol. 6, no. 4.
- [74] C. Cao and Y.-T. Long, “Biological nanopores: Confined spaces for electrochemical single-molecule analysis,” *Accounts of Chemical Research*, vol. 51, no. 2, pp. 331–341, 2018.
- [75] J. Nivala, D. B. Marks, and M. Akeson, “Unfoldase-mediated protein translocation through an a-hemolysin nanopore,” *Nature Biotechnology*, vol. 31, no. 3, pp. 247–250, 2013.
- [76] D. Rodriguez-Larrea and H. Bayley, “Multistep protein unfolding during nanopore translocation,” *Nature Nanotechnology*, vol. 8, no. 4, pp. 288–295, 2013.

- [77] C. C. Chau, S. E. Radford, E. W. Hewitt, and P. Actis, “Macromolecular crowding enhances the detection of dna and proteins by a solid-state nanopore,” *Nano Letters*, vol. 20, no. 7, pp. 5553–5561, 2020.
- [78] T. Gilboa and A. Meller, “Optical sensing and analyte manipulation in solid-state nanopores,” *The Analyst*, vol. 140, no. 14, pp. 4733–4747, 2015.
- [79] G. V. Soni, A. Singer, Z. Yu, Y. Sun, B. McNally, and A. Meller, “Synchronous optical and electrical detection of biomolecules traversing through solid-state nanopores,” *Review of Scientific Instruments*, vol. 81, no. 1, p. 014301, 2010.
- [80] T. Gilboa, C. Torfstein, M. Juhasz, A. Grunwald, Y. Ebenstein, E. Weinfeld, and A. Meller, “Single-molecule dna methylation quantification using electro-optical sensing in solid-state nanopores,” *ACS Nano*, vol. 10, no. 9, pp. 8861–8870, 2016.
- [81] S. Huang, M. Romero-Ruiz, O. K. Castell, H. Bayley, and M. I. Wallace, “High-throughput optical sensing of nucleic acids in a nanopore array,” *Nature Nanotechnology*, vol. 10, no. 11, pp. 986–991, 2015.
- [82] B. McNally, A. Singer, Z. Yu, Y. Sun, Z. Weng, and A. Meller, “Optical recognition of converted dna nucleotides for single-molecule dna sequencing using nanopore arrays,” *Nano Letters*, vol. 10, no. 6, pp. 2237–2244, 2010.
- [83] U. F. Keyser, B. N. Koeleman, S. van Dorp, D. Krapf, R. M. M. Smeets, S. G. Lemay, N. H. Dekker, and C. Dekker, “Direct force measurements on dna in a solid-state nanopore,” *Nature Physics*, vol. 2, no. 7, pp. 473–477, 2006.
- [84] S. Garaj, W. Hubbard, A. Reina, J. Kong, D. Branton, and J. A. Golovchenko, “Graphene as a subnanometre trans-electrode membrane,” *Nature*, vol. 467, no. 7312, pp. 190–193, 2010.
- [85] A. Smolyanitsky, B. I. Yakobson, T. A. Wassenaar, E. Paulechka, and K. Kroenlein, “A mos2-based capacitive displacement sensor for dna sequencing,” *ACS nano*, vol. 10, no. 9, pp. 9009–9016, 2016.

- [86] A. Arima, M. Tsutsui, T. Morikawa, K. Yokota, and M. Taniguchi, “Fabrications of insulator-protected nanometer-sized electrode gaps,” *Journal of Applied Physics*, vol. 115, no. 11, p. 114310, 2014.
- [87] N. Muthusubramanian, E. Galan, C. Maity, R. Eelkema, F. Grozema, and H. Van Der Zant, “Insulator-protected mechanically controlled break junctions for measuring single-molecule conductance in aqueous environments,” *Applied Physics Letters*, vol. 109, no. 1, p. 013102, 2016.
- [88] S. Tanimoto, M. Tsutsui, K. Yokota, and M. Taniguchi, “Dipole effects on the formation of molecular junctions,” *Nanoscale Horizons*, vol. 1, no. 5, pp. 399–406, 2016.
- [89] A. Bhat, P. V. Gwozdz, A. Seshadri, M. Hoeft, and R. H. Blick, “Tank circuit for ultrafast single-particle detection in micropores,” *Physical review letters*, vol. 121, no. 7, p. 078102, 2018.
- [90] A. Arima, M. Tsutsui, I. H. Harlisa, T. Yoshida, M. Tanaka, K. Yokota, W. Tonomura, M. Taniguchi, M. Okochi, T. Washio, *et al.*, “Selective detections of single-viruses using solid-state nanopores,” *Scientific reports*, vol. 8, no. 1, pp. 1–7, 2018.
- [91] M. N. Rhyner, “The coulter principle for analysis of subvisible particles in protein formulations,” *The AAPS Journal*, vol. 13, no. 1, pp. 54–58, 2010.
- [92] M. Kelleci, H. Aydogmus, L. Aslanbas, S. O. Erbil, and M. S. Hanay, “Correction: Towards microwave imaging of cells,” *Lab on a Chip*, vol. 18, no. 3, pp. 540–540, 2018.
- [93] S. Schmid, L. G. Villanueva, and M. L. Roukes, *Fundamentals of nanomechanical resonators*, vol. 49. Springer, 2016.
- [94] C.-Y. Cheng, J. Song, J. Pas, L. H. Meijer, and S. Han, “DmsO induces dehydration near lipid membrane surfaces,” *Biophysical Journal*, vol. 109, no. 2, pp. 330–339, 2015.

- [95] P. Kumari and H. K. Kashyap, “DmsO induced dehydration of heterogeneous lipid bilayers and its impact on their structures,” *The Journal of Chemical Physics*, vol. 151, no. 21, p. 215103, 2019.
- [96] V. Nerguizian, A. Alazzam, I. Stiharu, and M. Burnier, “Characterization of several cancer cell lines at microwave frequencies,” *Measurement*, vol. 109, pp. 354–358, 2017.
- [97] M. Yuksel, E. Orhan, C. Yanik, A. B. Ari, A. Demir, and M. S. Hanay, “Nonlinear nanomechanical mass spectrometry at the single-nanoparticle level,” *Nano letters*, vol. 19, no. 6, pp. 3583–3589, 2019.
- [98] A. K. Naik, M. Hanay, W. Hiebert, X. Feng, and M. L. Roukes, “Towards single-molecule nanomechanical mass spectrometry,” *Nature nanotechnology*, vol. 4, no. 7, pp. 445–450, 2009.
- [99] M. S. Hanay, S. Kelber, A. Naik, D. Chi, S. Hentz, E. Bullard, E. Colinet, L. Duraffourg, and M. Roukes, “Single-protein nanomechanical mass spectrometry in real time,” *Nature nanotechnology*, vol. 7, no. 9, p. 602, 2012.
- [100] M. S. Hanay, S. I. Kelber, C. D. O’Connell, P. Mulvaney, J. E. Sader, and M. L. Roukes, “Inertial imaging with nanomechanical systems,” *Nature nanotechnology*, vol. 10, no. 4, pp. 339–344, 2015.
- [101] J. E. Sader, M. S. Hanay, A. P. Neumann, and M. L. Roukes, “Mass spectrometry using nanomechanical systems: beyond the point-mass approximation,” *Nano letters*, vol. 18, no. 3, pp. 1608–1614, 2018.
- [102] J. S. Joseph, S. T. Malindisa, and M. Ntwasa, “Two-dimensional (2d) and three-dimensional (3d) cell culturing in drug discovery,” *Cell. Culture*, vol. 2, pp. 1–22, 2018.
- [103] H.-J. Park and D. M. Helfman, “Up-regulated fibronectin in 3d culture facilitates spreading of triple negative breast cancer cells on 2d through integrin β -5 and src,” *Scientific reports*, vol. 9, no. 1, pp. 1–14, 2019.

- [104] S. Trujillo, C. Gonzalez-Garcia, P. Rico, A. Reid, J. Windmill, M. J. Dalby, and M. Salmeron-Sanchez, “Engineered 3d hydrogels with full-length fibronectin that sequester and present growth factors,” *Biomaterials*, p. 120104, 2020.

Appendix A

Supplementary Materials for Cell Detection Part



Figure A.1: Photolithography mask used for cell detection & flow rate sensor

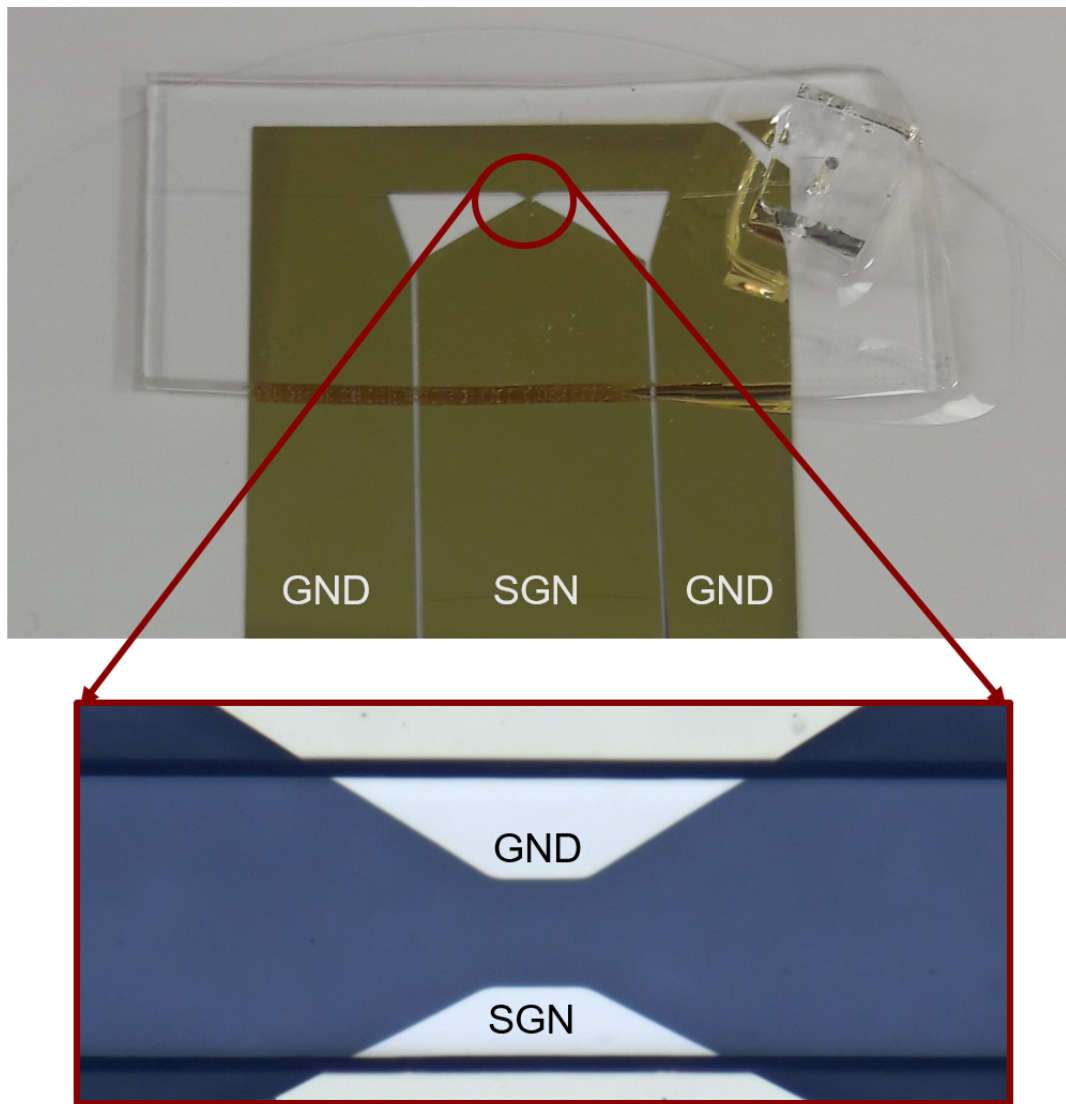


Figure A.2: An example of device after cleanroom fabrication

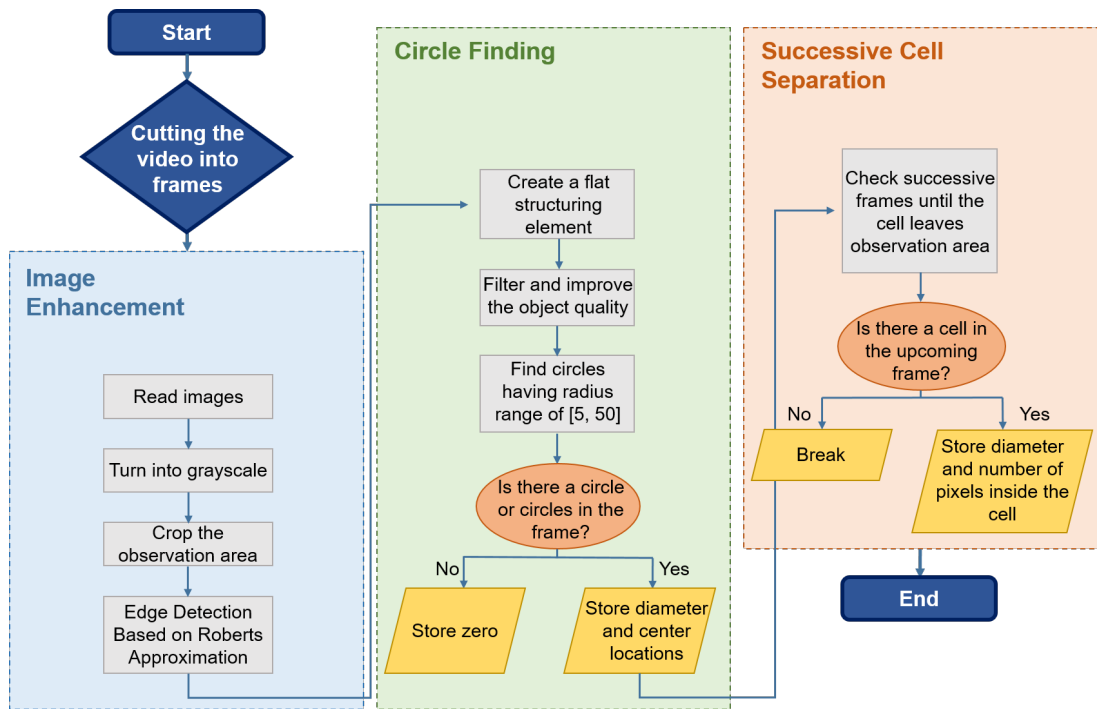


Figure A.3: Working steps of the custom-built image processing algorithm

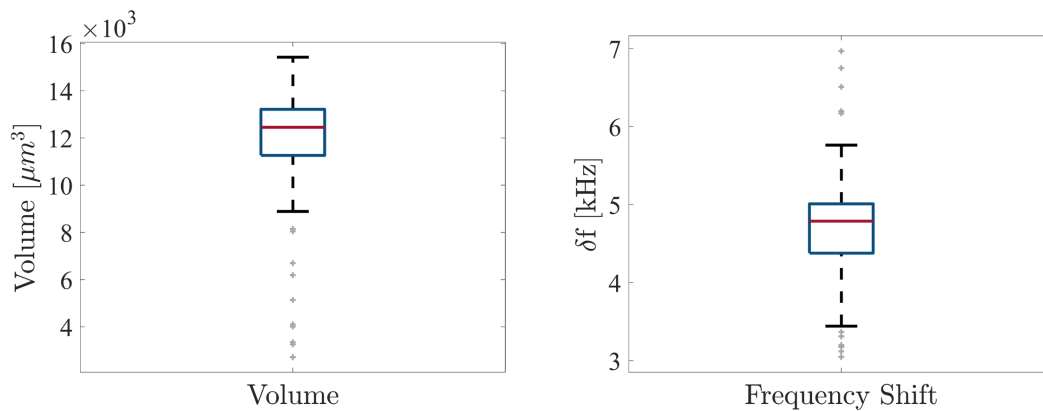


Figure A.4: Boxplots for the Histogram in Figure 2.12

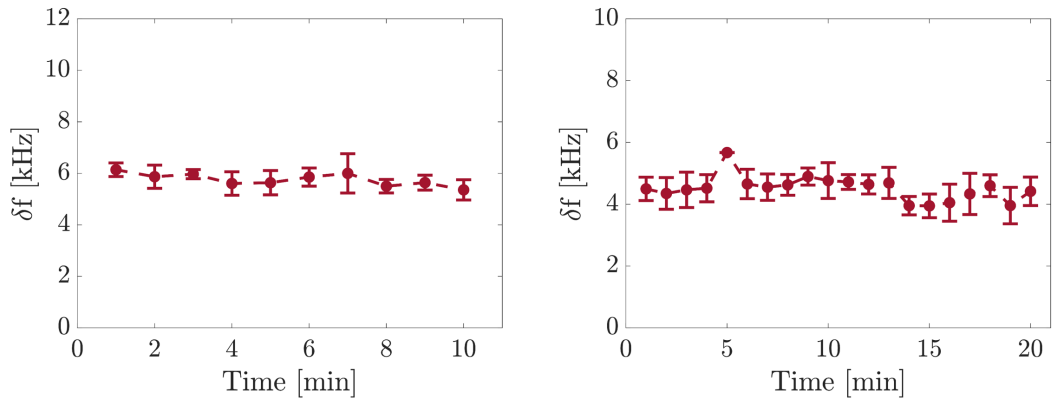


Figure A.5: Frequency shift trend obtained with different cells and devices

Appendix B

Supplementary Materials for Flow Sensor Part

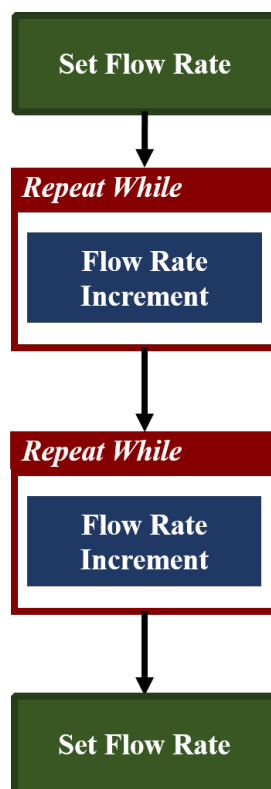


Figure B.1: An example of block diagram used for automatically adjusting flow rate using Fluigent software